Journal of Magnetic Resonance **136,** 176–199 (1999)
Article ID jmre.1998.1615, available online at http://www.idealibrary.com on IDEAL®

Modeling EPR Powder Spectra Using Numerical Diagonalization of the Spin Hamiltonian

Guillaume Morin*,[1] and Dominique Bonnin†

*Laboratoire de Minéralogie-Cristallographie, UMR C7590, Universités Paris 6 et 7 and IPGP, 4, place Jussieu, 75252 Paris Cedex 05, France;
†Laboratoire de Physique Quantique, ESA 7069, Ecole Supérieure de Physique et Chimie Industrielles,
10 rue Vauquelin, 75231 Paris Cedex 05, France

E-mail: morin@lmcp.jussieu.fr

Received May 28, 1998; revised September 15, 1998

A new modeling code, ZFSFIT (standing for Zero Field Splitting FITting), written in FORTRAN 77 is proposed. It is designed for computing and fitting EPR powder spectra described by any spin Hamiltonian including second- and fourth-order ZFS terms ($S \leq \frac{5}{2}$) and/or a hyperfine term ($I \leq \frac{7}{2}$). Based on numerical diagonalization of the spin Hamiltonian, this code computes the powder spectrum, the calculated angular dependencies, and the energy levels at any orientation. Least-squares refinement of the spin Hamiltonian parameters is performed either by adjusting powder line positions (EPRPLP module) or by directly fitting the powder spectra (ZFSFIT code). Especially, simultaneous fitting of EPR powder line positions recorded at distinct frequencies improves the accuracy of the refined EPR parameters. Superhyperfine effects as well as broadening effects due to site-to-site distribution of g-, A-, and ZFS parameters are treated using first-order perturbation theory and can also be refined. Parameters for several distinct centers can be fitted simultaneously, allowing quantification of their relative amounts in the sample. After a description of the algorithm, determination of second- and fourth-order ZFS parameters of Cr^{3+}, Mn^{2+}, and Fe^{3+} centers in low-symmetry sites in minerals are treated, including first evidence of structural Fe^{3+} centers in $\alpha Al(OH)_3$. The code is available without charge to academic users from the authors.

Key Words: **EPR; powder; computing; fitting; transition ions.**

1. INTRODUCTION

Electron paramagnetic resonance (EPR) spectroscopy, sometimes referred to as electron spin resonance spectroscopy (ESR), is a powerful tool used in several fields of physics, chemistry, and biochemistry (*1, 2*). Indeed, the low-level detection threshold (ppm) and the structural sensitivity of EPR allow analysis of the nature and localization of paramagnetic point defects (*3*) as well as the atomic environment of paramagnetic ions, mainly first-row transition ions and lanthanide ions, in various solids and liquids (*4, 5*). For instance, quantification of radiation-induced paramagnetic defects by EPR is used for dating and dosimetry (*3*). EPR is also used to study the site distribution of paramagnetic impurities in solids, as well as the relaxation processes related to their structural accommodation by the host matrix (*6–8*).

Single-crystal EPR analysis yields both the whole set of spin Hamiltonian parameters and the orientation of the principal axes of the local ligand field with respect to crystallographic axes. In polycrystalline solids, this relative orientation cannot be determined because an EPR powder spectrum is a summation over all orientations of the local ligand field with respect to the static applied field direction (*9*). The interpretation of the EPR powder spectra is then only based on the determination of the spin Hamiltonian parameters, whose values reflect the local symmetry of the paramagnetic center. Numerical integration of the EPR absorbance on the whole orientation sphere being time-consuming, interpretation and modeling of powder EPR spectra have been often treated using perturbation theory. Examples of automated fitting of EPR powder spectra for $S = \frac{1}{2}$ species, based on high order perturbation calculations, were given in a recent paper (*10*). In case of higher spin values ($S > \frac{1}{2}$), perturbation calculations are based on the relative importance of the zero field splitting (ZFS) and of the Zeeman splitting. Either strong magnetic field approximation ($ZFS \ll h\nu$) (*4, 11, 12*) or strong ligand-field approximation ($ZFS \gg h\nu$) (*13–15*) have been used for analyzing fine structure spectra of transition elements.

These approximations are, however, clearly inapplicable in the case of an intermediate ligand field ($ZFS \equiv h\nu$), as, for instance, for Fe^{3+} and Cr^{3+} ions in many oxides and silicates (*6*). High-order perturbation calculations (*16*) or straightforward numerical diagonalization of the spin Hamiltonian (see, for instance, *17–21*) are then required to determine reliable resonance fields values. For $S > \frac{3}{2}$, e.g., for S-state ions, the large number of allowed transitions occurring between and inside the Kramers' doublets, makes it difficult to index the EPR lines in powder studies (*22, 23*), and even in single-crystal studies (*24*). Furthermore, complex angular dependencies, observed for low site symmetry, can only be interpreted by including fourth-order ZFS terms (see, for instance, *24–27*),

[1] To whom correspondence should be addressed. Fax: 33 1 44 27 37 85.

1090-7807/99 $30.00

although these terms are still generally omitted in powder EPR studies (*19–23*). Fourth-order ZFS terms must, however, be taken into account to unambiguously distinguish between line-splitting due to complex angular dependencies and that related to the presence of distinct paramagnetic centers (see Section 4). For triclinic site symmetry, single-crystal EPR analysis of the relative orientations of the pseudo-symmetry axes of the fourth-order ZFS tensor with respect to those of the crystallographic coordination polyhedra is a powerful method for localizing paramagnetic impurities and for assessing local relaxation of the host structure (*8, 28–30*). Unfortunately, since orientation of the fourth-order ZFS axes cannot be determined from the EPR study of polycrystalline samples, physical interpretation of fourth-order terms derived from powder data is then restricted to the qualitative description of the site symmetry. The use of fourth-order terms, however, significantly improves the accuracy of second-order terms and is necessary for correctly modeling powder spectra, a striking point for quantifying relative amounts of distinct paramagnetic centers.

Successful attempts at computing EPR powder spectra of $S > \frac{3}{2}$ centers using numerical diagonalization of the spin Hamiltonian are reported in the literature (*17–21*). However, among these works, none deals with complex ($S = \frac{5}{2}$) centers in triclinic symmetry where all fourth-order ZFS terms are required. Moreover, no procedure have been proposed for fitting EPR powder data in such cases, although this facility offers the ability to fully determine the Hamiltonian parameters of unknown centers, as will be shown in Section 4.

The present computation code, based on numerical diagonalization of the full spin Hamiltonian, is designed for computing and fitting EPR powder spectra described by any spin Hamiltonian including fourth-order ZFS terms ($S \leq \frac{5}{2}$) and/or hyperfine structure ($I \leq \frac{7}{2}$). It constitutes a significant improvement for understanding the complex EPR powder spectra encountered when ZFS $\equiv h\nu$. After a definition of the spin Hamiltonian used (Section 2), the computation algorithm, the time-reducing optimizations and the modeling of EPR powder lineshapes will be detailed (Section 3). Fluctuations of the EPR parameter from site to site, which are very common features in natural and synthetic minerals, are taken into account and used as indicators of structural disorder. Then, it is shown, by analyzing EPR powder spectra of Fe^{3+} in some polycrystalline solids (Section 4), that the present code is a powerful tool for deriving accurate second- and fourth-order fine structure parameters from EPR powder data, as well as for assessing relative site occupancies of impurities in minerals.

2. DEFINITION OF THE SPIN HAMILTONIAN USED IN THE CODE

An EPR spectrum is due to electronic transitions between electronic-spin levels which are hard to calculate from the total Hamiltonian of an atom surrounded by atom neighbors, especially in low site symmetry. A solution of the problem lies in the use of a phenomenological Hamiltonian called the spin Hamiltonian. It is related to an effective spin S for the ground state such that the number of levels is $2S + 1$ (*4*).

We used the following spin Hamiltonian to describe the EPR spectra of ($S \leq \frac{5}{2}$; $I \leq \frac{7}{2}$) centers:

$$\mathbf{H} = \beta \mathbf{H} \cdot \mathbf{g} \cdot \mathbf{S} + \sum_{k=2,4} \sum_{q=-k}^{k} B_k^q \mathbf{O}_k^q + \mathbf{S} \cdot \mathbf{A} \cdot \mathbf{I}, \qquad [1]$$

where the three right-hand terms correspond to the Zeeman interaction, the quadrupole fine structure interaction and the hyperfine interaction.

In the Zeeman term, $\mathbf{g}$, β, $\mathbf{H}$, and $\mathbf{S}$ are the gyromagnetic tensor, the electronic Bohr magneton, the applied magnetic field vector, and the spin operator in the $2S + 1$ dimension space, respectively. The $\mathbf{g}$-tensor is generally anisotropic because of spin–orbit coupling.

The quadrupole fine structure term, which yields a partial removal of the primary $2S + 1$ degeneracy, i.e., the so-called zero-field splitting (ZFS), is related to indirect effects of ligand field and covalency on the spin states only if $S \geq 1$, and then reflects the local symmetry of the ligand field. The ZFS term can be expressed by a linear combination of polynomial operators of order k (with k even and $k \leq 2S + 1$) in S_x, S_y, S_z, having the same transformation properties as spherical harmonics. Operators with odd k values are not considered because they are not invariant with time reversal (*4*). Several definitions of these operators as well as various notations were used in the EPR literature, as extensively reviewed in (*31*). In the code proposed here, the Stevens operators (*32*), $\mathbf{O}_k^{\pm q}$, and the associated real Stevens constant, $B_k^{\pm q}$, were chosen because they are the most often used in the EPR literature (*4–7, 31–33*). Algebraic expressions of these operators for $k = 2$ and 4 and matrix elements of the ZFS term in the $S = \frac{5}{2}$ case are given in the Appendix.

When analyzing powder EPR spectra, by contrast with single-crystal EPR analysis, the relative orientation between crystallographic and ZFS principal coordinate frames cannot be assessed. In order to reduce the number of free parameters, the coordinate frame will be chosen such that the expression of the ZFS tensor is as simple as possible. The choice of the reference coordinate frame as a function of site symmetry, in the powder case, is discussed with the help of examples in Section 4. The general rule is that the principal axis frame of the second-order ZFS tensor is taken as the reference coordinate frame. When the site symmetry of the paramagnetic center is higher than monoclinic, second- and fourth-order principal coordinate frames coincide or are mutually related by axis permutations. In contrast, for monoclinic and triclinic site symmetries, principal axes of the second-order and fourth-order ZFS tensors do not coincide and angular dependencies may become complex. However, when the angle between the principal Z axes of the second- and fourth-order ZFS tensors, respectively, remains small, this rotation can be neglected. In such cases, the rota-

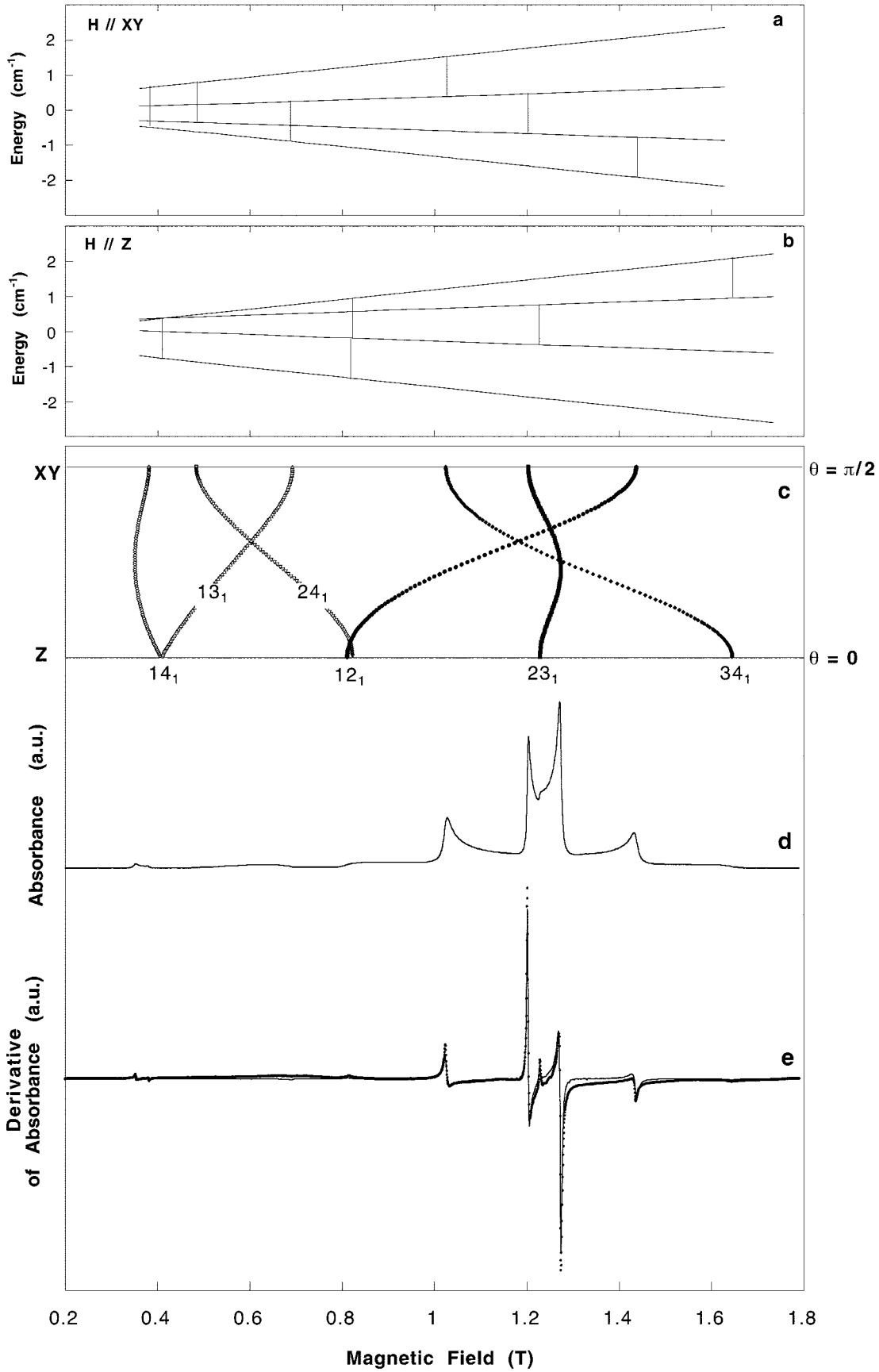
H // XY
a
Energy (cm-1)
2
1
0
-1
-2
H // Z
b
Energy (cm-1)
XY
Z
θ = π/2
θ = 0
c
13 1
24 1
14 1
12 1
23 1
34 1
Absorbance (a.u.)
d
Derivative of Absorbance (a.u.)
e
0.2
0.4
0.6
0.8
1
1.2
1.4
1.6
1.8
Magnetic Field (T)

tions of the fourth-order principal axes in the *XOY* plane are easily accounted for by the introduction of B_4^{-q} terms.

In the hyperfine term, **A**, **S**, and **I** are the hyperfine tensor, the electronic-spin operator in the 2S + 1 dimension space, and the nuclear-spin operator in the (2I + 1)-dimension space, respectively. The nuclear quadruple interaction $\mathbf{I} \cdot \mathbf{P} \cdot \mathbf{I}$ and the nuclear Zeeman interaction $\beta_N \mathbf{H} \cdot \mathbf{g}_N \cdot \mathbf{I}$ may be nonnegligible in some cases, and principal axes of the **g**-, **A**-, and ZFS tensors may significantly differ (*34–36*). However, implementing $\mathbf{I} \cdot \mathbf{P} \cdot \mathbf{I}$ and $\beta_N \mathbf{H} \cdot \mathbf{g}_N \cdot \mathbf{I}$ terms and all possible noncoincidences between principal axes of **g**, second-order ZFS, fourth-order ZFS, **A**, $\mathbf{g}_N$, and **P** tensors would yield a large number of free parameters, 3 + 5 + 9 + 6 + 6 + 5 = 34, per center in triclinic symmetry. Since present applications of our code focus on ZFS terms in low-symmetry cases, we reduced the maximum number of parameters to 3 + 2 + 9 + 3 = 17 per center in a triclinic crystal field by neglecting $\mathbf{g}_N$ and **P** terms and restricting **A** and **g** to be diagonal in the second-order ZFS principal axes. Under these assumptions, the Zeeman terms become $\beta \mathbf{H} \cdot \mathbf{g} \cdot \mathbf{S} = \beta H(g_x n_x S_x + g_y n_y S_y + g_z n_z S_z)$, where H is the magnetic field module, $n_x = \sin\theta \cos\phi$, $n_y = \sin\theta \sin\phi$, and $n_z = \cos\theta$ are the direction cosines of the magnetic field vector in second-order ZFS principal axes, and the hyperfine term is reduced to $\mathbf{S} \cdot \mathbf{A} \cdot \mathbf{I} = \mathbf{S}_x A_{xx} \mathbf{I}_x + \mathbf{S}_y A_{yy} \mathbf{I}_y + \mathbf{S}_z A_{zz} \mathbf{I}_z$. Nuclear quadruple interaction $\mathbf{I} \cdot \mathbf{P} \cdot \mathbf{I}$ and nuclear Zeeman interaction $\beta_N \mathbf{H} \cdot \mathbf{g}_N \cdot \mathbf{I}$ as well as off-diagonal terms of **g**- and **A**-tensors could be included in future versions of the code, taking advantage of the full diagonalization procedure.

3. COMPUTATION OF EPR POWDER SPECTRA

Reliable interpretation and least-squares fitting of EPR powder spectra require an accurate modeling of EPR powder lineshapes. Complex shapes may result both from the intrinsic EPR lineshapes of the individual transitions and from their angular dependencies.

3.1. Integration Scheme

An EPR powder spectrum can be considered as the summation of the spectra corresponding to every orientation $\{\theta, \phi\}$ of the applied magnetic field direction with respect to the principal coordinate system of the EPR center, whose Z axis is then taken as quantification axis. Each $\{\theta, \phi\}$ direction defines a distinct diagram of energy levels $E_m(H, \theta, \phi)$ and a distinct set of transitions (Fig. 1a, 1b). The function $H_{nm}(\theta, \phi)$, which describes the variations of the resonance field of a given nm transition as a function of the $\{\theta, \phi\}$, direction is the so-called angular dependency of this transition (Fig. 1c). For $\Delta m_s = \pm 1$ transitions, angular dependencies of transition probabilities, $I_{nm}(\theta, \phi)$, are much weaker than the angular dependencies of resonance field positions and have sometimes been neglected (*15*). However, transition probabilities are functions of $\{\theta, \phi\}$ and have to be computed to yield the right intensities, especially for weakly allowed transitions. For each transition, the summation on the orientation sphere yields steps or peaks in the absorbance function (Fig. 1d) when the first derivative of the angular dependency with respect to θ or ϕ vanishes. In an EPR powder spectrum, observed lines only correspond to these particular $\{\theta, \phi\}$ directions, often called "turning points" (*18*) since the spectrum is experimentally recorded as the derivative of the absorbance function with respect to magnetic field strength (Fig. 1e). Therefore, the smoothness of a computed EPR powder spectrum crucially depends on the size and the number of the elementary solid angles, taken into account in the summation. As a consequence, optimization of the space partition is critical for reducing computation time.

Various partitioning schemes, performing the integration over a set of approximately equal solid angles, have been proposed in the literature for modeling magnetic resonance powder spectra. Those include the "igloo" method (*17*) used in the QPOW code, a spiral integration method (*37*), an equilateral triangular partition (*38*) and, more recently, the SOPHE method based on a triangular partition with elementary triangular sections having exactly the same solid angle (*19*).

It is now well accepted these methods have at least two main advantages with respect to a classical partition using a $\{\theta, \phi\}$ square network with constant θ and ϕ steps:

(i) The number of computed orientations is severely reduced since each solid angle has approximately or exactly similar sections. This avoids the excessive computations arising from classical square grid partitions, when varying ϕ for small values of θ (*38*).

(ii) They do not introduce any divergence in the absorbance intensity when θ approaches zero. This is not the case in the square grid partition, where the contribution of each solid angle has to be weighted by sin θ (*38*).

In addition, triangular partitions are more suitable for fast interpolation algorithms, i.e., two-dimensional linear interpolation in (*38*) and one-dimensional spline interpolations in the SOPHE method (*19*), than the "igloo" method (*17*), which requires nonlinear two-dimensional interpolations. Finally, triangular partitions where the integration grid is completely defined (*19, 38*) are preferable to the spiral method (*37*) where nodes are determined at each angular step using a minimizing routine, as discussed in (*19*).

It is also important to remark that since energy levels are generally sorted and indexed as increasing energy value (*17–*

FIG. 1. Direct least-squares fitting of the *Q*-band spectrum (ν = 34.004 GHz) at 300 K of the Cr^{3+} center in synthetic polycrystalline ruby (0.03 wt% Cr_2O_3). (a) Spin levels along X or Y; (b) spin levels along Z; observed transitions are indicated by vertical lines; (c) angular dependencies in the ZOX plane, where transitions are labeled nm_p; (d) computed absorbance function; (e) EPR powder spectra: dotted line: experimental spectrum; plain line: computed spectrum, with $g_{xy} = 1.9778$; $g_z = 1.9807$; $B_2^0 = -0.0623$ cm^{-1}; $\sigma_{B_2^0} = 0.002$ cm^{-1}; and $\Gamma_0 = 0.0035$ T.

21, 37, 38), it is necessary to ensure that transitions do not involve any crossing levels when using interpolations for evaluating angular dependencies (*17–19, 37, 38*), unless the interpolated resonance field values may not be actually relative to the "same" transition along the interpolation range, as mentioned by some authors (*18, 37, 38*). This problem becomes crucial when using nonlinear interpolation methods, e.g., over a whole "$\theta\phi$" curve in the SOPHE method (*19*), especially for computing weakly allowed transitions occurring when $h\nu \equiv$ ZFS, as pointed out by Van Veen (*18*). On the contrary, even if the linear interpolation scheme of Alderman *et al.* (*38*) appears to be less advanced that other methods based on nonlinear interpolations, it offers the ability to generate the absorbance function relative to each elementary triangle independently from the data computed for other directions. Therefore, the crossing of two levels within an elementary triangular solid angle does not affect the absorbance functions computed within other elementary solid angles. In addition, appropriate computation of line broadening, by taking into account the slope of the energy levels as a function of H, allows local errors on transition indices to be compensated in some cases. These aspects are detailed in Section 3.5.

As a consequence, in the present code, the number of computed orientations is minimized by using the partitioning and interpolating scheme developed by Alderman *et al.* (*38*). It was originally devoted to compute NMR powder spectra and has not yet been used for modeling EPR powder spectra. In this model, the summation is performed over the faces of a regular octahedron placed so that its six vertices lie along the coordinate axes, at unit distances from the origin. Each face of the octahedron is partitioned to form a grid of $N(N + 1)/2$ small equilateral triangles having the same area, where N is referred to as the partition number. Thus, any vertex of any of these small triangles, corresponding to a particular $\{\theta, \phi\}$ orientation, can be easily indexed by two integers, i and j. The direction cosines describing the magnetic field vector from the origin to the grid intersection are directly obtained from the indices i and j, without recourse to time-consuming trigonometric function evaluation. The solid angle weighting factor for any small triangle is approximated by $1/R^3$, where R is the distance from the origin to the small triangle. The small error relative to this approximation becomes negligible when the partition number N is increased, and it was shown in (*38*) that this method yields the exact spectrum shape, generally with $N \leq 125$, depending on the anisotropy of the angular dependencies.

3.2. Computing Resonance Fields and Transition Intensities

The algorithm of Alderman *et al.* (*38*) was written for modeling NMR powder spectra, where the resonance frequencies and the intensities of the transitions depend only on the orientation of the magnetic field, since its strength is constant. Finding the NMR frequencies, for a given orientation, then only requires solving one eigenproblem of dimension n, where n is the dimension of the nuclear spin Hamiltonian. In contrast, EPR experiments are performed by sweeping magnetic field at constant frequency. As a consequence, for each $\{\theta, \phi\}$ orientation, the eigenproblem has to be solved as a function of the magnetic field strength. This complex issue can be expressed as a super-operator problem where resonance fields are solution of an n^2 generalized eigenproblem, where $n = [1, 2, \ldots, (2S + 1)(2I + 1)]$ is the dimension of the electron spin Hamiltonian (*39*). We first checked this algebraic method by using the HGEEV routine (*40*) to solve the generalized Hermitian eigenproblem of dimension n^2. Despite the fact that this method is efficient when n is smaller than 8, it becomes more than four times slower than the method we present below, when the n value increases. In addition, the degeneracy of the eigenvalues of the super-operator makes it difficult to compute transition probabilities. Another way to find the resonance field would consist in systematically computing eigenvalues $E_m(H)$ of the spin Hamiltonian for all H values, and then looking for transitions between computed levels. This procedure is, however, time-consuming since the Hamiltonian is mostly diagonalized for nonresonance fields values.

In the present code, we propose an efficient method consisting of automatically converging on resonance field values, using a recursive routine based on Newton dichotomy. For a given $\{\theta, \phi\}$ orientation, this routine, referred to as SEARCH, computes resonance fields H_{nm} (Figs. 1a, 1b) and intensities I_{nm} of every nm transition, without making any excess diagonalization.

The SEARCH routine can be described as follows. Minimum and maximum values of the magnetic field ($H_{\min}$ and $H_{\max}$, respectively) are taken as starting boundary values for the search interval $[H_A, H_B]$. The ZHEEV routine (*40*), designed for diagonalizing Hermitian matrix (double precision complex), is called for computing eigenvalues, $E_n(H_A)$, $E_n(H_B)$, and $E_n(H_C)$, where $H_C = \frac{1}{2}(H_A + H_B)$ and $n = [1, 2, \ldots, (2S + 1)(2I + 1)]$. The occurrence of transition(s) in the $[H_A, H_C]$ and in the $[H_C, H_B]$ intervals is checked by testing if the $h\nu$ value lies within the range $[\Delta E_{mn}(H_A), \Delta E_{mn}(H_C)]$ and $[\Delta E_{mn}(H_C), \Delta E_{mn}(H_B)]$, respectively, where $\Delta E_{mn}(H) = |E_n(H) - E_m(H)|$. This condition is satisfied for $[H_A, H_C]$ if the sign of the product $P_{AC} = [h\nu - \Delta E_{mn}(H_A)][h\nu - \Delta E_{mn}(H_C)]$ is negative, and for $[H_C, H_B]$ if the sign of the product $P_{CB} = [h\nu - \Delta E_{mn}(H_C)][h\nu - \Delta E_{mn}(H_B)]$ is negative. If this condition is satisfied for one or both $[H_A, H_C]$ and $[H_C, H_B]$ intervals, the SEARCH routine calls itself with $[H_A, H_C]$ and/or $[H_C, H_B]$ intervals as new $[H_{A'}, H_{B'}]$ search interval. This recursive search is performed until H_A and H_B values both converge on the same resonance field value. The SEARCH routine returns when the $|H_B - H_A|$ value becomes lower than 1/10 of the experimental field step size used for measuring and computing the spectrum. Such accuracy in resonance-field values is necessary for constraining interpolated resonance-field values.

In case of crossing n and m levels, the searching method outlined above may fail because a transition may occur on each side of the crossing point (see Section 3.5). Hence, despite two transitions occurring within the same $[H_A, H_C]$ or $[H_C, H_B]$ interval, the condition on the negative sign of the products P_{AC} or P_{CB}, respectively, is not satisfied. An additional condition has then to be added. The simplest way to circumvent this difficulty is to keep on searching transitions until the $|H_B - H_A|$ value becomes lower than a limit value H_{limit}, whatever the signs of the P_{AC} and P_{CB} are. In practice, this limit value has to be small enough that every transition is found, and as large as possible in order to reduce computing time. Actually, the choice of this limit value depends on the complexity of the energy level diagram. If the ZFS terms are small with respect to Zeeman terms, energy levels do not cross each other and the limit value is taken as infinite. On the other hand, if the ZFS terms are of the same order of magnitude as the Zeeman term, energy levels often cross each other, and the limit value may be as low as 0.05 T at Q-band.

These remarks show that, for a given orientation, a transition between given m and n levels can occur at more than one resonance field value in the magnetic field domain investigated, as already mentioned in (*18*). Resonance fields have then to be labeled in all cases as $H_{nm_p}(\theta, \phi)$, where p is the rank of the resonance field for the nm transition. $H_{nm_p}(\theta, \phi)$ functions, i.e., angular dependencies, can be plotted for all occurring transitions (Fig. 1c). This output is of prime importance in order to index the experimental EPR powder lines.

Once a resonance field H_{nm_p} value has been determined for a given $\{\theta, \phi\}$ direction, the ZHEEV subroutine is called for computing the eigenvectors of the spin Hamiltonian at H_{nm_p}, in order to calculate transition intensity.

Transition intensities between n and m energy levels are computed according to (*41, 18*), considering that the microwave oscillating magnetic field $\boldsymbol{H}_1$ is perpendicular to the applied magnetic field $\boldsymbol{H}$,

$$\begin{aligned} I_{nm} = {} & (1 - \sin^2\theta \cos^2\phi) S^*_{x_{nm}} S_{x_{nm}} \\ & - \sin^2\theta \sin\phi \cos\phi [S^*_{x_{nm}} S_{y_{nm}} + S^*_{y_{nm}} S_{x_{nm}}] \\ & - \cos\theta \sin\theta \cos\phi [S^*_{x_{nm}} S_{z_{nm}} + S^*_{z_{nm}} S_{x_{nm}}] \\ & + (1 - \sin^2\theta \sin^2\phi) S^*_{y_{nm}} S_{y_{nm}} \\ & - \cos\theta \sin\theta \sin\phi [S^*_{y_{nm}} S_{z_{nm}} + S^*_{z_{nm}} S_{y_{nm}}] \\ & + \sin^2\theta \cdot S^*_{z_{nm}} S_{z_{nm}} \end{aligned} \qquad [2]$$

with $S_{k_{mn}} = \langle V_m | S_k | V_n \rangle$, where V_m and V_n are the eigenvectors corresponding to levels m and n, respectively, and S_k is a spin operator, S_x, S_y, or S_z.

3.3. Computing Lineshapes

Once features originating from the powder problem are accurately modeled, physical origin of the EPR lineshapes has to be taken into account. The classical single-orientation EPR lineshape can be affected by many parameters, including experimental ones and intrinsic ones. The intrinsic width and shape of EPR transitions are actually constrained by both dynamic and static causes that lead to homogeneous and nonhomogeneous broadening, respectively. Dynamic processes occurring in the EPR experiment can be approached by the Bloch model (*1*). In this model, the line profile is the classical first derivative normalized Lorentzian curve, whose linewidth depends on both the spin–lattice and spin–spin relaxation times, τ_1 and τ_2, respectively.

On the other side, unresolved superposition of spectral components can yield nonhomogeneous broadening:

(i) Unresolved superhyperfine coupling with neighboring odd nuclear spins (e.g., ^{1}H, ^{27}Al, ^{31}P, ^{29}Si . . .), which can be approximated by a Gaussian broadening of the lineshape (*1*).

(ii) Long-range spin–spin interaction, equivalent to a magnetic field heterogeneity which may generate significant line broadening (*4, 42*).

(iii) Short-range (super-) exchange interaction (via the ligands), between electronic spin of nearest neighbors (e.g., clusters), generally modeled by an exchange Hamiltonian associated with two Zeeman terms. For instance, it is written as follows for two interacting spins:

$$\beta \mathbf{H} \cdot g \cdot \mathbf{S}_1 + \beta \mathbf{H} \cdot g \cdot \mathbf{S}_2 + \mathbf{S}_1 \cdot \mathbf{J} \cdot \mathbf{S}_2, \qquad [3]$$

where $\mathbf{J}$ is the exchange tensor. This interaction, not introduced in the present version of our code, yields specific resonance lines, especially observed for ion pairs in minerals (*43, 44*).

(iv) Slight variations of the electronic environment from site to site, at equivalent crystallographic position. Those may be modeled by local deviations of the spin Hamiltonian parameters and yield complex anisotropic line broadening. When these deviations are small, they can be approximated by a Gaussian distribution, the resulting line broadening being computed using first-order perturbation theory (*45*).

Broadening effects due to site-to-site distribution of Hamiltonian parameters may yield useful information on long-range disorder and structural relaxation phenomena. Therefore, in the code proposed, the opportunity to take into account small distribution of any parameter of a ($S \leq \frac{5}{2}$, $I \leq \frac{7}{2}$) spin Hamiltonian $\mathbf{H}$, i.e., g_{ij}, $B_k^{\pm q}$ and A_{ij} parameters, was included. The distribution of each Hamiltonian parameter (e.g., B_2^0) is characterized by a perturbation quantity (e.g., $\sigma_{B_2^0}$). Theses perturbation quantities are simultaneously considered as a unique perturbation Hamiltonian referred to as $\mathbf{H}_S$. The full Hamiltonian is then written as

$$\mathbf{H} = \mathbf{H}_0 + \mathbf{H}_S, \qquad [4]$$

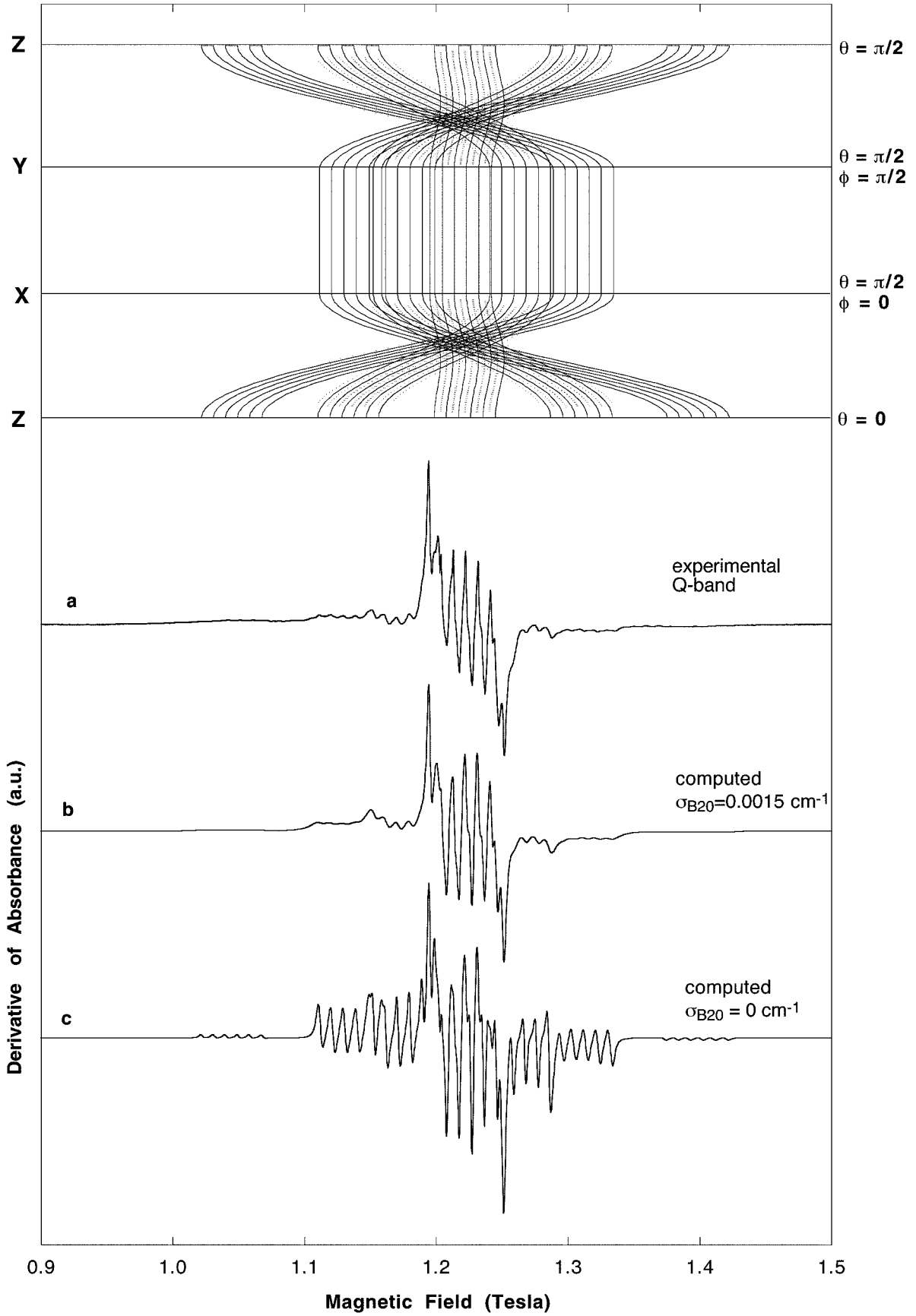
Z
Y
X
Z
θ = π/2
θ = π/2
φ = π/2
θ = π/2
φ = 0
θ = 0
a
experimental
Q-band
b
computed
σB20=0.0015 cm-1
c
computed
σB20 = 0 cm-1
Derivative of Absorbance (a.u.)
0.9
1.0
1.1
1.2
1.3
1.4
1.5
Magnetic Field (Tesla)

where $\mathbf{H}_0$ is the unperturbed Hamiltonian. As explained in Section 3.1, the SEARCH routine yield the resonance field and the transition intensity of every transition for a given orientation, using full diagonalization of the $\mathbf{H}_0$ Hamiltonian. For a given transition, involving n and m levels, the variations ΔE_n and ΔE_m of energy levels due to $\mathbf{H}_S$ are computed using the first-order perturbation theory, assuming that the perturbation is small (e.g., $\sigma_{B_2^0} \ll B_2^0$),

$$\Delta E_n = \langle V_n|\mathbf{H}_S|V_n\rangle \text{ and } \Delta E_m = \langle V_m|\mathbf{H}_S|V_m\rangle, \qquad [5]$$

where V_n and V_m are the eigenvectors of $\mathbf{H}_0$ directly obtained from the last iteration of the SEARCH routine. The resulting perturbation on the resonance field position of the nm_p transition, referred to as $\Gamma_{S_{nm_p}}$ is then calculated assuming that the energy levels are locally linear as a function of H,

$$\Gamma_{S_{nm_p}}(\theta, \phi) = 2 \cdot |\Delta E_m - \Delta E_n| \partial E_m/\partial H - \partial E_n/\partial H|^{-1}, \quad [6]$$

where $\partial E_m/\partial H$ and $\partial E_n/\partial H$ are the local slopes of the energy levels at the resonance field H_{nm_p}, those being readily obtained from the two last iterations of the SEARCH routine. The $\Gamma_{S_{nm_p}}(\theta, \phi)$ value obtained from Eq. [6] is readily considered as the strain contribution to the full-width-at-half-maximum (FWHM), assuming that the broadening effect is symmetrical when the Hamiltonian parameters deviate in a positive or a negative sense (e.g., $\pm\ \sigma_{B_2^0}$), this assumption being consistent with Eq. [5] where the perturbation of the energy levels are calculated at first order.

Other broadening effects, e.g., unresolved superhyperfine interactions and magnetic dipolar broadening, are modeled by a unique constant and nonzero linewidth Γ_0, in the field domain. The total FWHM in the field domain, including Γ_0 and Γ_S, was assumed to have the form

$$\Gamma_{nm_p}(\theta, \phi) = [\Gamma_0^2 + \Gamma_{S_{nm_p}}^2(\theta, \phi)]^{1/2}. \qquad [7]$$

This expression, only correct in the pure Gaussian case, was found to give reasonable results in other cases studied.

Actually, Eq. [6] only holds when the energy levels are linear within the linewidth interval in the field domain. It may not be true at low field when $h\nu \equiv$ ZFS and/or when $h\nu \equiv A$. In these cases, even a symmetric broadening in the energy (frequency) domain rigorously generates an asymmetric broadening in the field domain, as pointed out by Pilbrow *et al.* (*46*), who give appropriate analytical expressions allowing this transformation to be computed. However, despite the fact that using these expressions requires no more computing time than classical convolution processes for a single EPR line, the necessity to generate the partial absorbance spectrum of each nm_p transition at each $\{\theta, \phi\}$ orientation severely increases the computing time when dealing with powder spectra. Therefore, in order to save computing time, Eq. [6] was used. It yields an alternative way to transform linewidth quantities from the energy domain to the field domain when the linewidth is small enough in the field domain. Moreover, the $\Gamma_{S_{nm_p}}(\theta, \phi)$ quantity obtained from Eq. [6] reasonably estimates the linewidth of the nm_p transition, when the Hamiltonian parameters deviate around their mean values, provided that these deviations are small.

For example, Fig. 2 shows the effect of a small site distribution on the EPR spectrum of Mn^{2+} ions substituted for Ca^{2+} ions at the Ca(1) site within the apatite structure (*47–49*). Comparison between the experimental spectrum (Fig. 2a) and the spectrum computed with a constant linewidth (Fig. 2c) indicates that resonance lines corresponding to transitions between $\langle m_S = \pm\frac{5}{2},\ m_I|$ and $|m_S = \pm\frac{3}{2},\ m_I\rangle$ levels, as well as between $\langle m_S = \pm\frac{3}{2},\ m_I|$ and $|m_S = \pm\frac{1}{2},\ m_I\rangle$ levels, are broadened. In contrast, the transition between $\langle m_S = -\frac{1}{2},\ m_I|$ and $|m_S = +\frac{1}{2},\ m_I\rangle$ levels is not broadened. In first-order perturbation approximation, it is expected that small variations in the B_2^0 value do not affect transitions occurring between energy levels with equal m_S absolute value (*45*). The existence of such small fluctuations of the local environment of Mn^{2+} ions in the apatite structure is strongly supported by the agreement between the experimental spectrum and that computed by including a Gaussian distribution of the B_2^0 value with $\sigma_{B_2^0} = 0.0015\ \text{cm}^{-1}$ (Fig. 2b). These site-to-site modifications may be interpreted as a signature of the structural accommodation of the size mismatch between Mn^{2+} and Ca^{2+} ions (*47*). In the same way, a recent application of our code showed that it is very suitable for modeling strain effects on the g factors of radiation-induced defect centers in glasses (*50*).

3.4. Building the Powder Spectrum

Once resonance fields, transition intensities, and linewidths are computed and stored separately for each nm_p transition and for every vertex of the triangular grid, i.e., for every orientation of $\mathbf{H}$ with respect to the ZFS axis frame, powder absorbance functions relative to each nm_p transition are computed according to the linear interpolation scheme of Alderman *et al.* (*38*) (Fig. 1c).

It is important to note that the term "interpolation" is actually not fully suitable for characterizing the algorithm of these authors. This method drastically differs from a simple linear interpolation procedure consisting of generating a large num-

FIG. 2. Direct least-squares fitting of the Q-band spectrum ($\nu = 34.200$ GHz) at 300 K of Mn^{2+} ions at the Ca(1) site in natural apatite from Treguenec (France). Upper part: angular dependencies; plain lines: $\Delta M_I = 0$ transitions; dotted lines: $\Delta M_I = \pm 1$ transitions, forbidden along the principal axes. Lower part: (a) experimental spectrum; (b) computed spectrum with $\sigma_{B_2^0} = 0.0015\ \text{cm}^{-1}$ and $\Gamma_0 = 0.004$ T; (c) computed spectrum with $\sigma_{B_2^0} = 0\ \text{cm}^{-1}$ and $\Gamma_0 = 0.004$ T.

ber of Dirac delta functions from the three sets of resonance fields and transition intensities exactly computed at the three vertices of the elementary triangle, as proposed, for instance, for the local linear interpolation procedure within the subpartition of the SOPHE method (*19*). In contrast, for each transition, the algorithm developed by Alderman *et al.* (*38*) generates the absorbance function by "distributing" the average intensity within the elementary triangle as a "tent" shape lying in the $[H_{\min}, H_{\max}]$ interval, where $H_{\min}$ and $H_{\max}$ are the minimum and maximum values of the angular dependency of the resonance field within the elementary triangle, respectively. For a given mn_p transition and a given triangle q, the area of this triangular "tent" is taken proportional to the arithmetic average $I_{nm_p}(q)$ of the transition intensity at the three vertices of the triangle, since angular dependence of the transition intensity is generally small within the triangle. This method significantly smoothes the absorbance function and gives the exact spectrum shape (*38*) with much smaller partition number values than other methods based on the summation of Dirac delta functions.

The partial absorbance functions, relative to each nm_p transition, are separately stored in order to be separately convoluted, because, as shown in Section 3.3, the linewidth may vary from one transition to another and as a function of the **H** direction.

Because of the Γ_S component, the total linewidth depends both on the n and m spin states involved in the nm_p transition, and on the $\{\theta, \phi\}$ direction. However, local convolution of the absorbance function relative to each transition, for each direction or for each elementary triangle using the average of the linewidth over the three vertices (*19*), is extremely time-consuming. In the present code, for each nm_p transition, the average $\Gamma_{nm_p}(q)$ of the linewidth over the three vertices of each triangle q is computed in a first step. However, in order to save computing time, the anisotropic broadening effect over the whole orientation sphere is then approximated by a linewidth quantity $\bar{\Gamma}_{nm_p}(H)$, being only a function of the magnetic field strength, for a given transition. The main issue for determining $\bar{\Gamma}_{nm_p}(H)$ arises from the nonbijective character of some angular dependencies. For instance, for a given nm_p transition, when considering two distinct triangles referred to as 1 and 2, the interval of interpolated resonance field values $[H_{\min}, H_{\max}]_{(1)}$ and $[H_{\min}, H_{\max}]_{(2)}$, corresponding to the two triangles, respectively, often overlap, although $\Gamma_{nm_p}(1) \neq \Gamma_{nm_p}(2)$ and $I_{nm_p}(1) \neq I_{nm_p}(2)$. This difficulty was circumvented by computing, for each nm_p transition and for each interpolated H value, an average linewidth value $\bar{\Gamma}_{nm_p}(H)$, weighted by transition intensities:

$$\frac{1}{\bar{\Gamma}_{nm_p}(H)} \sum_{q=1}^{q_{\max}} I_{nm_p}(q) \Bigg|_H = \sum_{q=1}^{q_{\max}} \frac{I_{nm_p}(q)}{\Gamma_{nm_p}(q)} \Bigg|_H, \qquad [8]$$

where $q_{\max}$ is the number of triangles which give the same interpolated resonance field H for the same nm_p transition. Therefore, once $\bar{\Gamma}_{nm_p}(H)$ is only a function of H for each nm_p transition, the absorbance function of each nm_p transition can be separately convoluted at the end of the calculation, the full-width $\bar{\Gamma}_{nm_p}(H)$ of the profile shape function varying as a function of H. A linear combination of normalized Gaussian and Lorentzian functions (pseudo-Voigt function) was chosen as the line-profile function, since the lineshape resulting from the various broadening effects outlined above is generally neither pure Lorentzian nor Gaussian. In practice, the first derivative of absorbance for each nm_p transition is readily obtained by convoluting the corresponding absorbance functions, with a normalized first-derivative pseudo-Voigt function $dpV(H)$ with FWHM $\Gamma = \bar{\Gamma}_{nm_p}(H)$ and having the form

$$\begin{aligned} dpV(H) = {} & (1 - \alpha)(-16H\pi^{-1}\Gamma^{-3})[1 + 4H^2\Gamma^{-2}]^{-2} \\ & + \alpha(-16[\ln(2)]^{3/2}H\pi^{1/2}\Gamma^{-3}) \\ & \times \exp(-4\ln(2)H^2\Gamma^{-2}), \end{aligned} \qquad [9]$$

where α is an adjustable parameter in the [0, 1] interval. For convenience, the full-width $\bar{\Gamma}_{nm_p}(H)$ have been taken as similar for the Lorentzian and Gaussian components. Finally, the classical EPR spectrum is obtained by summing the first-derivative spectra of all nm_p transitions.

3.5. Remarks on Crossing Levels

It is important to remember that interpolation methods imply the need to "keep track of the transitions so that the proper values are used to interpolate each transition calculated," as pointed out by Mombourquette and Weil (*37*). Van Veen (*18*) used a sorting procedure based on the continuity of the derivatives of the angular dependency, but he remarked that "an exact calculation of the resonance field and of the transition intensity had to be substituted to the interpolated values for the angular intervals where the correspondence between the transitions cannot be established reliably." More generally, it can be inferred from the work of Kato (*51*) that there is no suitable method for sorting wavefunctions, such as the angular dependency $H(\theta, \phi)$ of every transition can be described as a differentiable function. Therefore, the simple ascending order sorting is generally preferred, although it fails in some special cases which can be classified as two types:

(i) "Looping" transitions (*18, 46*): There may exist $\{\theta, \phi\}$ directions where two levels n and n' behave in such a way that $0 < |E_n - E_{n'}| < h\nu$ in a particular H interval and $|E_n - E_{n'}| \geq h\nu$ outside of this interval. In that case, one transition appears at each extremity of the interval, and these two transitions are indexed as nn'_p and nn'_{p+1} in our algorithm. However, this situation does not correspond to a true crossing when the condition $|E_n - E_{n'}| > 0$ is verified. Moreover, since $|E_n - E_{n'}|$ vary as a function of $\{\theta, \phi\}$, angular dependencies of nn'_p and nn'_{p+1} transitions can coalesce at a particular $\{\theta, \phi\}$ orientation, i.e., coalescence point, such as $0 < |E_n - E_{n'}| = h\nu$. Finally, the nn' transition may disappear when $|E_n - E_{n'}|$

TABLE 1
Nonzero ZFS Parameters and Integration Domain Required for Computing the EPR Powder Spectrum of S = 2 and S = $\frac{5}{2}$ Centers, as a Function of Site Symmetry[a]

Symmetry	Nonzero ZFS parameters	Integration domain
Cubic	$a/120 = B_4^0 + 5B_4^4$ [b]	X, Y, Z
	$a/120 = B_4^0 + 20\sqrt{2}\, B_4^3$ [c]	X, Y, Z
Hexagonal	B_2^0, B_4^0	X, Y, Z
Quadratic	B_2^0, B_4^0, B_4^4	X, Y, Z
Trigonal	B_2^0, B_4^0, B_4^3	$X, Y, Z; -X, Y, Z$
Orthorhombic	$B_2^0, B_2^2, B_4^0, B_4^2, B_4^4$	X, Y, Z
Monoclinic	$B_2^0, B_2^2, B_4^0, B_4^2, B_4^{-2}, B_4^4, B_4^{-4}$	$X, Y, Z; -X, -Y, Z$
Triclinic	$B_2^0, B_2^2, B_4^0, B_4^1, B_4^{-1}, B_4^2, B_4^{-2}, B_4^3, B_4^{-3}, B_4^4, B_4^{-4}$	$X, Y, Z; -X, Y, Z; -X, -Y, Z; X, -Y, Z$

[a] X, Y and Z refer to the principal axes of the second-order ZFS tensor and are taken as the reference coordinate frame. The **g** and **A** tensors are considered to be diagonal in this coordinate frame.
[b] Z along a fourfold axis.
[c] Z along a threefold axis.

$> h\nu$. Such an nn' transition is called a "looping" transition because its angular dependency forms a loop. Looping transitions occur when $h\nu \equiv$ ZFS (see, for instance, 24_{1-2}, 34_{2-3}, and 45_{1-2} transitions in the X-band spectrum of αAl_2O_3:Fe^{3+}, Fig. 3), rather than when $h\nu \gg$ ZFS (Q-band spectrum of αAl_2O_3:Fe^{3+}, Fig. 4). In our algorithm, since nn'_p and nn'_{p+1} transitions are indexed separately, they are not interpolated one with each other at the coalescence point and two undesirable steps appear in the absorbance functions of both transitions. However, when computing broadening effects as strain effects, using Eq. [6] or more appropriate expressions from (*46*), the field domain linewidths of nn'_p and nn'_{p+1} transitions become very large when their angular dependencies coalesce, because the slopes of the n and n' energy levels vanish at this point, as was experimentally observed (*52*). Therefore, the computed EPR spectrum is smooth, even if the two branches of the loop have not been interpolated through the coalescence point (see, for instance, transitions 24_{1-2}, 34_{2-3}, and 45_{1-2} in Fig. 3 and transitions 23_{1-2}, 34_{2-3}, and 45_{1-2} in Fig. 5).

(ii) "True crossing": There may exist particular (θ, ϕ) directions where a resonance field H_{nm} involves two degenerate levels n and n' such as $|E_n - E_{n'}| = 0$. In such points, referred to as "true crossing" points, the angular dependency of all transitions involving the n or n' level cannot be simultaneously differentiable, whatever procedure has been chosen for sorting eigenvalues. Indeed, for a given $\{\theta, \phi\}$ orientation and using an appropriate sorting order for the energy levels, eigenvalues of the Hamiltonian can be described by analytical functions of H because the spin Hamiltonian is linear in H (*51*). However, the appropriate sorting order may differ for an adjacent $\{\theta, \phi\}$ orientation if at least two levels cross each other. Consequently, using such sorting procedures yields discontinuities in the angular dependencies at "true crossing" points. Besides, when energy levels are sorted in ascending order, a "true crossing" generates an undesirable "repulsive" feature on the angular dependencies of transitions involving the crossing levels, as observed for transitions 24_2 and 23_2 in Fig. 6, when levels 3 and 4 cross each other on the axis. However, it can be inferred from the work of Von Neumann and Wigner (*53*) that such true crossing can only occur at isolated points of the (θ, ϕ) space, generally corresponding to high symmetry directions. Consequently, when using the interpolation algorithm of Alderman *et al.*, the contribution of a discrete "true crossing" point to the powder spectrum is small because it only affects a single elementary triangle among the $N(N + 1)/2$ triangles, where typically $15 \leq N \leq 125$.

4. REFINEMENT OF EPR PARAMETERS

4.1. General Method

The spin Hamiltonian parameters (g_{ij}, B_k^q, A_{ij}) define the resonance fields and intensities of each transition for every $\{\theta, \phi\}$ direction of the magnetic field **H**. Since powder spectra average all possible orientations of the applied magnetic field direction, relative to the ZFS axis frame, powder lines only occur when one of the first derivatives of the angular dependence function, as a function of θ or ϕ respectively, vanishes for a given transition. Each line of a powder spectrum is then related to a particular $\{\theta, \phi\}$ direction of the magnetic field vector **H** where a nm_p transition has a stationary angular dependency ("turning point") (Figs. 1, 2, and 3). As a consequence, any line of a powder spectrum, at an H_{nmp} field position, is indexed by nm_p and a $\{\theta, \phi\}$ direction. S and I values and site symmetry of the paramagnetic center constrain the number of Hamiltonian parameters required for describing the EPR spectrum, as well as the domain of integration required for computing the EPR powder spectrum (Table 1). An overview of the definition and use of the spin Hamiltonian in low symmetry systems is given in (*54*). In cases where **g** and **A** tensors are not diagonal in the same coordinate frame, complex situations may occur (see, e.g., *34*), but these will not be discussed here.

Determination of the Hamiltonian parameters from the ex-

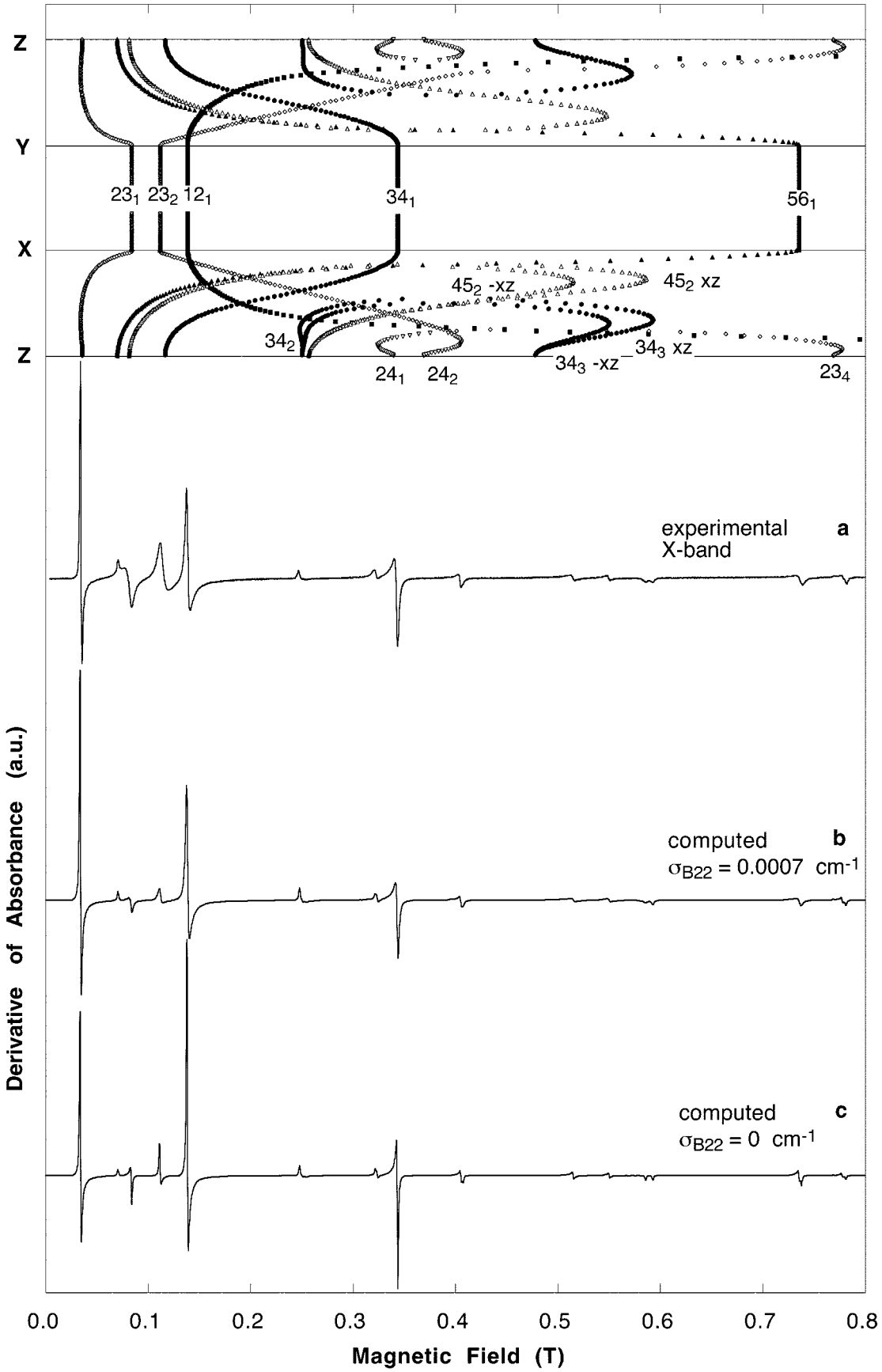
Z
Y
X
Z
23_1 23_2 12_1
34_1
56_1
45_2 -xz
45_2 xz
34_2
34_3 -xz
34_3 xz
24_1 24_2
23_4
experimental
X-band
a
computed
σ_{B22} = 0.0007 cm^{-1}
b
computed
σ_{B22} = 0 cm^{-1}
c
Derivative of Absorbance (a.u.)
0.0 0.1 0.2 0.3 0.4 0.5 0.6 0.7 0.8
Magnetic Field (T)

TABLE 2
EPR Parameters (cm^{-1}) of Mn^{2+} Center at Ca(1) Site in Fluoroapatite

g	B_2^0 (cm^{-1})	A_{xy} (cm^{-1})	A_z (cm^{-1})	Temp. (K)	References
2.0002	0.0138	0.0087	0.0087	300	This study
2.0005	0.0133	0.0086	0.0088	300	*47*
1.9919	0.0133	0.0086	0.0089	300	*48*
2.0000	0.0157	0.0086	0.0086	77	*49*

TABLE 3
ZFS Parameters (cm^{-1}) of Fe^{3+} Center at Al^{3+} Site in Corundum at 300 K

B_2^0	$60B_4^0$	$60B_4^3$	Reference
0.0561	−0.0110	0.2181	This study
0.0559	−0.0110	0.2198	*57*

Note. g value is taken isotropic at 2.0000.

perimental spectrum can be conducted by the two following steps:

First, the spin Hamiltonian parameters can be adjusted in order to minimize the sum of the squares of the differences between observed and calculated positions of selected powder lines, using a separate module referred to as EPRPLP.

Second, the Hamiltonian parameters, the line-profile parameters, and the scale factors can be adjusted by a direct full-spectrum fitting procedure, i.e., minimizing the sum of the squares of the difference between the experimental and calculated EPR intensities, over every point of the spectrum. This second option is performed by the main code ZFSFIT, which uses the same input file as EPRPLP.

In both codes, the same least-squares minimizing routine, LMDER1 (*55*), based on the Levenberg–Marquardt algorithm, is used.

Full-spectrum fitting, however, requires the set of initial parameters to be close to the solution. An initial refinement, using selected line positions, is then generally required, and the crucial step of this analysis consists in indexing powder lines. This task may become extremely difficult when dealing with two or more paramagnetic centers with high S values and low site symmetries. Indeed, for a given S (and I) center, the lower the site symmetry is, the higher the number of powder lines and the more complex the angular dependencies are. Moreover, it is important to remark that, in the general case, e.g., triclinic symmetry, the "turning point" directions of a transition in the symmetry planes (e.g., *ZOX*, *XOY*, *YOZ* . . .) generally depend on the spin Hamiltonian parameters and do not correspond to the principal axes of the EPR center. As a consequence, possible changes in the "turning point" directions have to be taken into account when fitting line positions. The initial "turning point" directions can be determined by comparing the experimental spectrum with a computed spectrum and the corresponding angular dependencies computed in the symmetry planes. Changes in "turning point" directions can be assessed by comparing experimental powder data with a set of spectra and angular dependencies computed with various Hamiltonian parameters.

For instance, rough estimation of the second-order ZFS parameters can generally be obtained by adjusting X-band line positions. The refined parameters can then be used to compute the corresponding X- and Q-band powder spectra. Indexing remaining experimental lines is then possible even when complex angular dependencies are observed, using angular dependencies computed in the symmetry planes. Better accuracy in the definition of the Hamiltonian parameters can be achieved by including these line positions and associated "turning points" in the refinement procedure. Accurate second- and fourth-order ZFS parameters can be extracted from powder data, using this feedback approach, i.e., indexing—refinement—spectra computation, as demonstrated by the examples given below.

4.2. No ZFS Term

For $S = \frac{1}{2}$, no ZFS parameters are defined. As a consequence, the axis frame where the **g**-tensor is diagonal, i.e., the principal axis frame of the **g**-tensor, is preferably taken as reference coordinate frame. In that case, the indexing procedure is simple, since the $\{\theta, \phi\}$ directions of the powder lines always coincide with the reference coordinate axes. Therefore, the computation of the spectrum can be restricted to one-eighth of the integration sphere, i.e., the (X, Y, Z) face of the octahedron defined in Section 3.1.

4.3. Second-Order ZFS Terms

For $S > \frac{1}{2}$ and whatever the site symmetry, there exists a set of orthonormal axes, X, Y, and Z, such that B_2^1, B_2^{-1} and B_2^{-2} terms vanish and such that $|B_2^0| \geq |B_2^2|$. This axis frame, called the principal axis frame of the second-order ZFS tensor, is chosen as the reference coordinate system for all computations in the following text, although the code proposed includes B_2^1, B_2^{-1}, and B_2^{-2} terms, if needed. When $S > \frac{1}{2}$, several cases have to be distinguished, depending on the possible use of the fourth-order ZFS tensor.

FIG. 3. Experimental and calculated X-band powder spectra at 300 K of Fe^{3+} ions at Al sites in an iron-doped polycrystalline corundum (0.025 wt% Fe_2O_3). Upper part: angular dependencies where transitions are labeled nm_p; lower part: (a) experimental spectrum; (b) computed spectrum with $\sigma_{B_2^2} = 0.0007$ cm^{-1} and $\Gamma_0 = 0.0015$ T; (c) computed spectrum with $\sigma_{B_2^2} = 0$ cm^{-1} and $\Gamma_0 = 0.0015$ T.

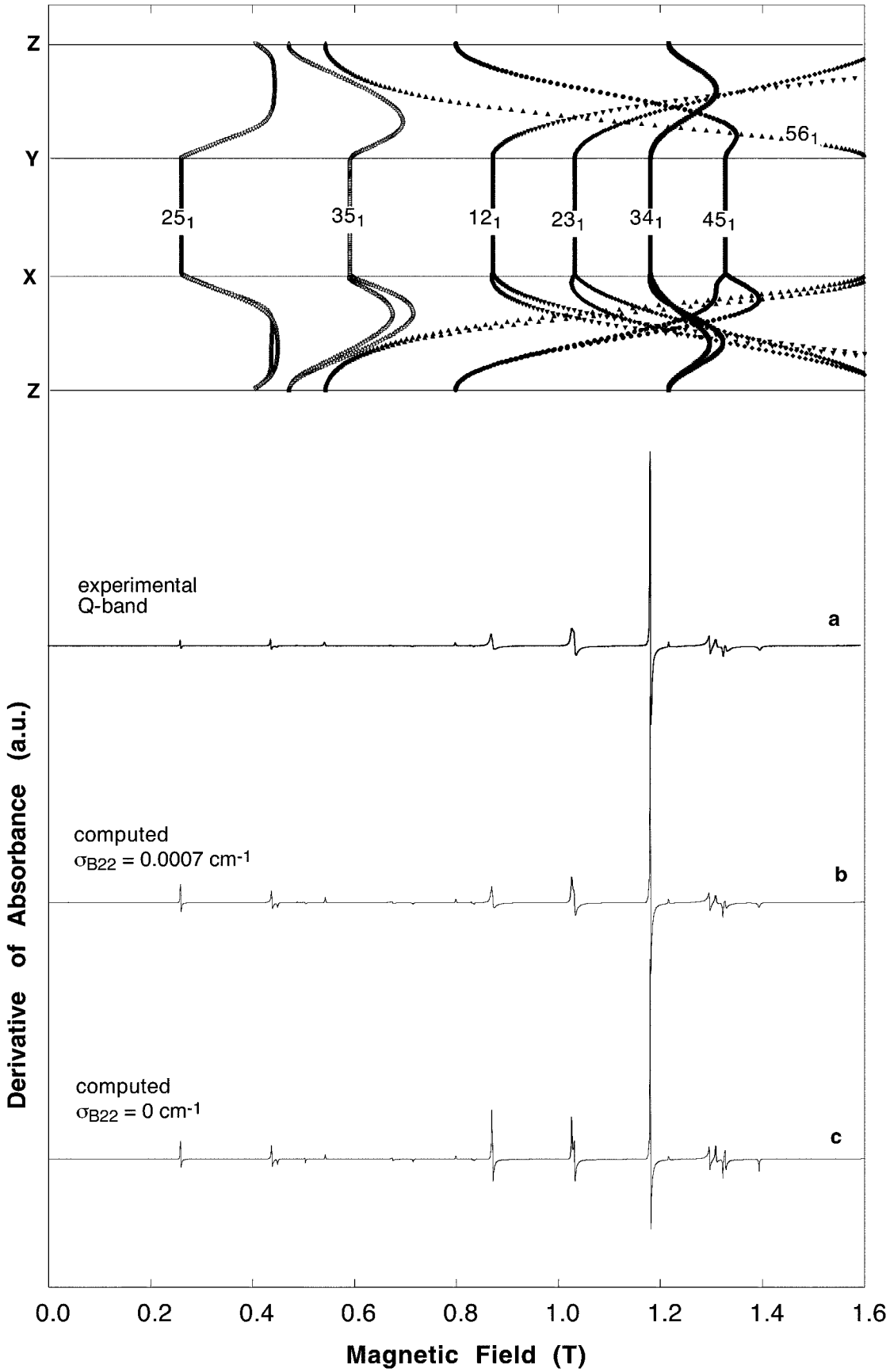
Z
Y
X
Z
25_1
35_1
12_1
23_1
34_1
45_1
56_1
experimental
Q-band
a
computed
σ_{B22} = 0.0007 cm^{-1}
b
computed
σ_{B22} = 0 cm^{-1}
c
Derivative of Absorbance (a.u.)
0.0
0.2
0.4
0.6
0.8
1.0
1.2
1.4
1.6
Magnetic Field (T)

TABLE 4
Experimental and Calculated Line Positions (Tesla) for Fe^{3+} Center at Al^{3+} Site in a Synthetic Corundum at 300 K

Transition		*X*-band (ν = 9.7768 GHz)		*Q*-band (ν = 34.0603 GHz)	
nm_p	[θ, ϕ]	Exp.	Calc.	Exp.	Calc.
12_1	*X*	0.1379	0.1384	0.8713	0.8712
12_1	*Y*			0.8713	0.8712
13_1	*Z*	0.0707	0.0717		
14_1	*X*			0.2595	0.2594
23_1	*X*	0.0839	0.0840	1.0329	1.0320
23_2	*X*	0.1120	0.1120		
23_1	(6, 0)	0.7801	0.7782		
23_1	(30, 0)	0.0339	0.0339		
24_1	(9, 0)	0.3226	0.3240		
25_1	(30, 180)			0.4477	0.4494
34_1	*X*	0.3436	0.3437	1.1813	1.1806
34_1	*Z*			1.2164	1.2161
34_1	(35, 0)			1.3235	1.3227
34_1	(35, 180)			1.2965	1.2962
34_2	(20, 0)	0.2469	0.2482		
34_3	(29, 0)	0.5928	0.5920		
34_3	(27, 180)	0.5494	0.5500		
45_1	*X*			1.3289	1.3280
36_1	*X*			0.5029	0.5038
45_1	*Z*			0.7978	0.7989
45_2	(66, 0)	0.5859	0.5862		
45_2	(63, 180)	0.5146	0.5150		
45_1	(70, 0)			1.3961	1.3935
56_1	*X*	0.7389	0.7356		
56_1	*Z*			0.5413	0.5430

For $S = 1$ or $S = \frac{3}{2}$, the second-order ZFS tensor only is defined. The [θ, ϕ] directions of the powder lines, i.e., turning points, generally coincide with the reference coordinate axes, i.e., principal axes of the second-order ZFS tensor, as for Cr^{3+} ($S = \frac{3}{2}$) ions (Fig. 1). Since the fourth-order ZFS tensor is expressed in its principal axes, the exact computation of the spectrum can be restricted to the (*X*, *Y*, *Z*) face of the octahedron. Besides, when the ZFS terms have the same order of magnitude as the Zeeman term (e.g., *56*), [θ, ϕ] directions of some powder lines may not coincide with any principal axis. That is clearly shown in Fig. 1, where the sharp 23_1 transition is stationary around the {90, 41} orientation. This remark sheds light on the necessity to take into account the possible change in orientation of the "turning points" of the transitions when adjusting ZFS parameters for fitting line positions. When directly fitting the full spectrum, this problem is obviously less crucial because powder lines are obtained from numerical integration.

For $S > \frac{3}{2}$, second- and fourth-order ZFS tensors may both be nonzero. When fourth-order ZFS terms are sufficiently small to be neglected, as for Mn^{2+} ($S = \frac{5}{2}$, $I = \frac{5}{2}$) at the Ca(1) site in apatite with site symmetry -3 (Table 2, Fig. 2), the {θ, ϕ} directions of the powder lines generally coincide with the reference coordinate axes, i.e., the principal axes of the second-order ZFS tensor, and the exact computation of the spectrum can be restricted to the (*X*, *Y*, *Z*) face of the octahedron. On the contrary, when fourth-order ZFS terms significantly contribute to the fine structure, complex angular dependencies may be observed and the domain of integration may have to be extended, especially for trigonal, monoclinic, and triclinic point symmetries.

4.4. Fourth-Order ZFS Terms

Table 1 recalls the ZFS parameters and domain of integration required for computing the powder spectrum as a function of site symmetry. This table is constructed in agreement with the conventions used in the code, i.e., the principal axes of the second-order ZFS tensor are chosen as the reference coordinate system.

In case of cubic, hexagonal, and quadratic site symmetries, the computation of the spectrum can be restricted to the (*X*, *Y*, *Z*) face of the octahedron, because the fourth-order ZFS tensor can be expressed in its principal axes, which coincide with those of the second-order ZFS tensor.

4.4.1. Trigonal site symmetry: Fe^{3+} in αAl_2O_3 (corundum). For trigonal site symmetry, only B_2^0, B_4^0 and B_4^3 parameters are nonzero. The *Z* axis lies along the unique crystallographic threefold axis and the *X* axis is chosen such that B_4^{-3} vanishes. In that case, the exact computation of the spectrum can no longer be restricted to the (*X*, *Y*, *Z*) face of the octahedron, and integration also has to be done over the ($-X$, *Y*, *Z*) face. Although angular dependencies are similar in the *YOZ* and $-YOZ$ planes, angular dependencies of several transitions may differ between the *ZOX* and *ZO* $-$ *X* planes, due to the trigonal symmetry of the $\mathbf{O}_4^3$ operator. An interesting example of this effect is given by the EPR spectra of Fe^{3+} substituted at the Al^{3+} octahedron with site symmetry *3* in the corundum structure, αAl_2O_3 (Tables 3 and 4): at X band (Fig. 3), the 34_3 {29, 0} and 34_3 {27, 180} lines are separated by 0.0434 T, and the 45_2 {66, 0} and 45_2 {63, 180} lines are separated by 0.0713 T; at *Q* band (Fig. 4), the 34_1 {35, 0} and 34_1 {35, 180} lines are separated by 0.0270 T. In the case of Fe^{3+} in corundum, the adjustment of these line positions at both *Q*-band and *X*-band frequencies allows accurate determination of the B_4^3 fourth-order parameter, in agreement with single-crystal EPR data (*57*) (Table 3). In addition, direct fitting of the *X*-band powder spectrum (Figs. 3a, 3b) indicated that the underestimation of the

FIG. 4. Experimental and calculated *Q*-band powder spectra at 300 K of Fe^{3+} ions at Al^{3+} sites in an iron-doped polycrystalline corundum (0.025 wt% Fe_2O_3). Upper part: angular dependencies where transitions are labeled nm_p; lower part: (a) experimental spectrum; (b) computed spectrum with $\sigma_{B_2^2} = 0.0007$ cm^{-1} and $\Gamma_0 = 0.002$ T; (c) computed spectrum with $\sigma_{B_2^2} = 0$ cm^{-1} and $\Gamma_0 = 0.002$ T.

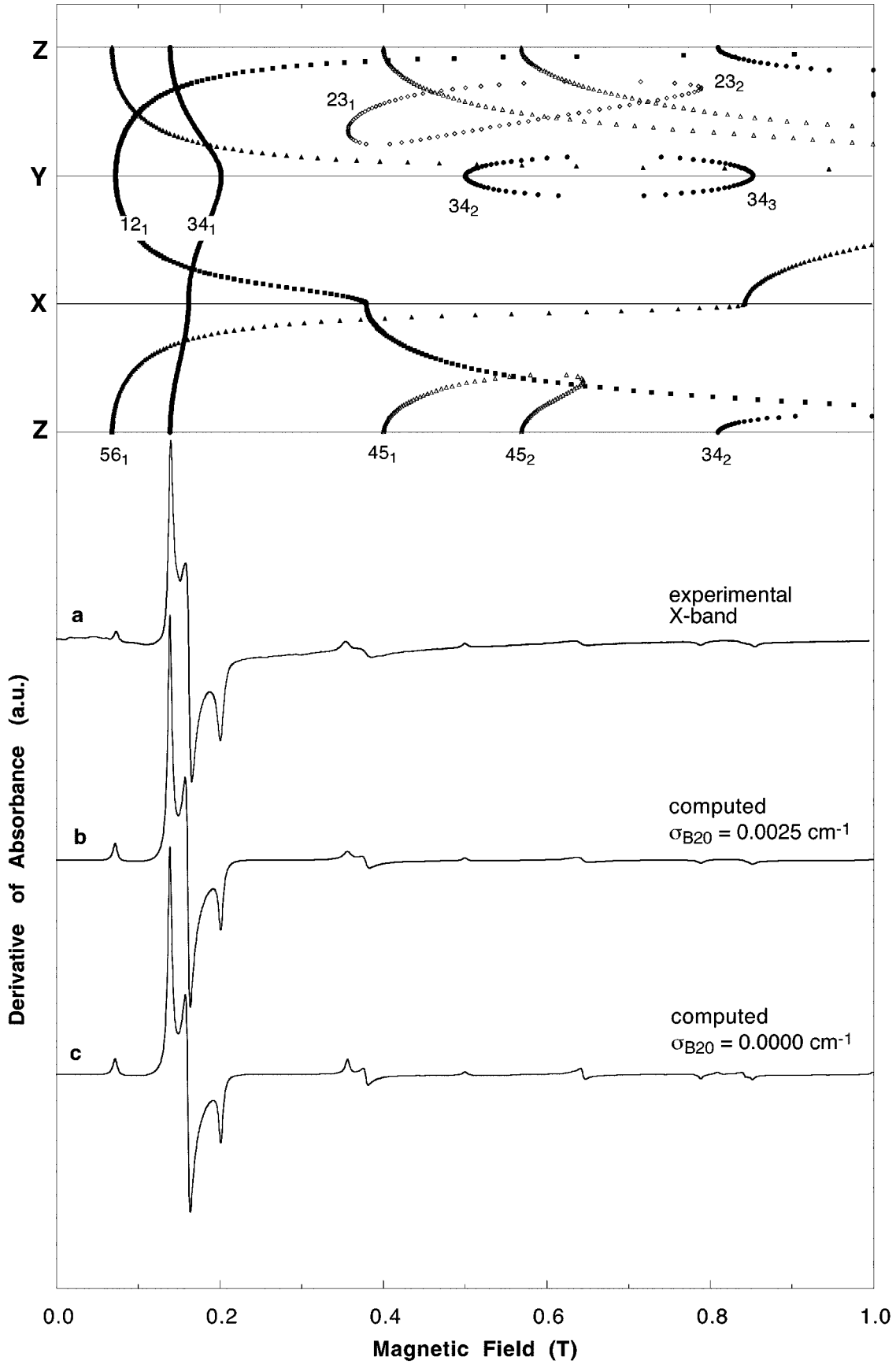
Z
Y
X
Z
23_1
23_2
34_2
34_3
12_1
34_1
56_1
45_1
45_2
34_2
a
experimental
X-band
b
computed
σ_{B20} = 0.0025 cm^{-1}
c
computed
σ_{B20} = 0.0000 cm^{-1}
Derivative of Absorbance (a.u.)
0.0
0.2
0.4
0.6
0.8
1.0
Magnetic Field (T)

TABLE 5
EPR Parameters (cm^{-1}) of Fe^{3+} Center at Al^{3+} Site in Diaspore

B_2^0	B_2^2	$60B_4^0$	$60B_4^2$	$60B_4^4$	Temp. (K)	Reference
0.1505	0.0982	0.0120	−0.0095	−0.0588	120	This study[a]
0.1473	0.0967	0.0126	−0.0160	−0.0514	300	(*59*)[b]

Note. g value is taken isotropic at 2.0000.
[a] Absolute sign of B_2^0 was not determined.
[b] Original ZFS parameters reported in (*59*) have been transformed into the same coordinate frame as in the present study, i.e., Z axis along the unique b-axis (*Pbnm* space group) using the rotation matrices given in (*31*).

relative intensity of the 23_1 Z with respect to 34_1 Z and 34_1XY lines (Fig. 3c) could only be corrected by including a small fluctuation around the axial symmetry (*58*), i.e., including $\sigma_{B_2^2} = 0.0007\ cm^{-1}$ (Fig. 3b). This result suggests that structural accommodation of Fe^{3+} for Al^{3+} substitution decreases the site symmetry of the host site. The underestimated intensities of the 23_1XY and 23_2XY lines are still not explained, but may be attributed to a failure of Eq. [1] and [2] for accurately calculating intensities of weakly allowed transitions in some cases. However, fitting of the X-band spectrum recorded at 120 K (data not shown), where 23_1XY and 23_2XY lines disappear because B_2^0 slightly increases, yields a better agreement than that in Fig. 3 and fully supports the existence of a nonzero $\sigma_{B_2^2}$ term.

4.4.2. Orthorhombic and monoclinic site symmetry: Fe^{3+} in αAlOOH (diaspore). In the case of orthorhombic site symmetry, only B_2^0, B_2^2, B_4^0, B_4^2, and B_4^4 parameters are nonzero. The Z axis, lying along the crystallographic twofold axis where $|B_2^0|$ is maximum, corresponds to a twofold axis of the second- and fourth-order ZFS tensors. The X axis is chosen such that B_2^{-2}, B_4^{-2}, and B_4^{-4} simultaneously vanish and the computation of the spectrum can be restricted to the (X, Y, Z) face of the octahedron. For all the point symmetries listed above, principal axis frames of the second- and fourth-order ZFS tensors coincide or are related by axis permutations. For lower point symmetries, this is no longer the case.

In the case of monoclinic site symmetry, only B_2^0, B_2^2, B_4^0, B_4^2, B_4^{-2}, B_4^4, and B_4^{-4} parameters are nonzero. The Z axis lies along the unique crystallographic twofold axis, but no X axis can be found such that B_2^{-2}, B_4^{-2}, and B_4^{-4} simultaneously vanish. According to the convention used in the present code, the X axis is chosen such that B_2^{-2} vanishes. It is then a twofold axis of the second-order ZFS tensor, but does not correspond to any symmetry axis of the fourth-order ZFS tensor. As a consequence, either B_4^{-2} or B_4^{-4} or both are nonzero. This situation corresponds to the noncoincidence, in the XOY plane only, of the second- and fourth-order principal axis frames. As a consequence, the integration domain has to be extended to the ($-X$, $-Y$, Z) face of the octahedron.

An interesting example of monoclinic site symmetry is given by the EPR spectra of Fe^{3+} substituted at the Al^{3+} site with site symmetry m, in the diaspore structure, αAlOOH. The Fe^{3+} center in diaspore was first studied in (*59*), where ZFS parameters obtained from single-crystal EPR data are reported (Table 5). As explained in (*59*), a particularity of the diaspore structure is that, although there is a unique crystallographic Al site, the (010) mirror (in Pbnm SG) yield two sets of magnetically nonequivalent Fe^{3+} sites. As a consequence, EPR single-crystal spectra of diaspore exhibit two Fe^{3+} centers in equal proportions, with the same site symmetry, but with distinct orientations with respect to the crystallographic coordinate frame. This difficulty is not encountered when analyzing EPR powder data, where the two distinct orientations of the Fe^{3+} centers contribute to the same powder spectrum. In the present study, ZFS parameters of the Fe^{3+} center in diaspore were refined by adjusting simultaneously 19 line positions from X- and Q-band powder data (Table 5). The good agreement between experimental and calculated line positions (Table 6), as well as between experimental and computed powder spectra at X-band (Fig. 5) and Q-band (Fig. 6), validates the accuracy of the refined ZFS parameters of the present study, even at fourth order. At Q-band, underestimation of the intensities of the 23_1 and 23_2 lines near the Z-direction may be related to preferential orientation along the b-axis/Z-axis direction. The correctness of the refined ZFS parameters is also supported by the consistency between the present study and the single-crystal study (*59*) (Table 6) and previous X-band powder spectrum simulations (*18*). Therefore, the present study confirms that the noncoincidence between the second- and fourth-order principal axes remain small, as already suggested (*59*). This "pseudo"-coincidence explains why a

FIG. 5. Experimental and calculated X-band powder spectra at 120 K of Fe^{3+} ions at Al site in natural diaspore from Turkey. Upper part: angular dependencies where transitions are labeled nm_p; lower part: (a) experimental spectrum; (b) computed spectrum with $\sigma_{B_2^0} = 0.0025\ cm^{-1}$ and $\Gamma_0 = 0.005$ T; (c) computed spectrum with $\sigma_{B_2^0} = 0\ cm^{-1}$ and $\Gamma_0 = 0.005$ T. Note that "looping" transitions, 23_{1-2}, 34_{2-3}, and 45_{1-2}, do not give rise to any "glitch" at the coalescence point in the spectrum computed with strain effect (see Section 3.5).

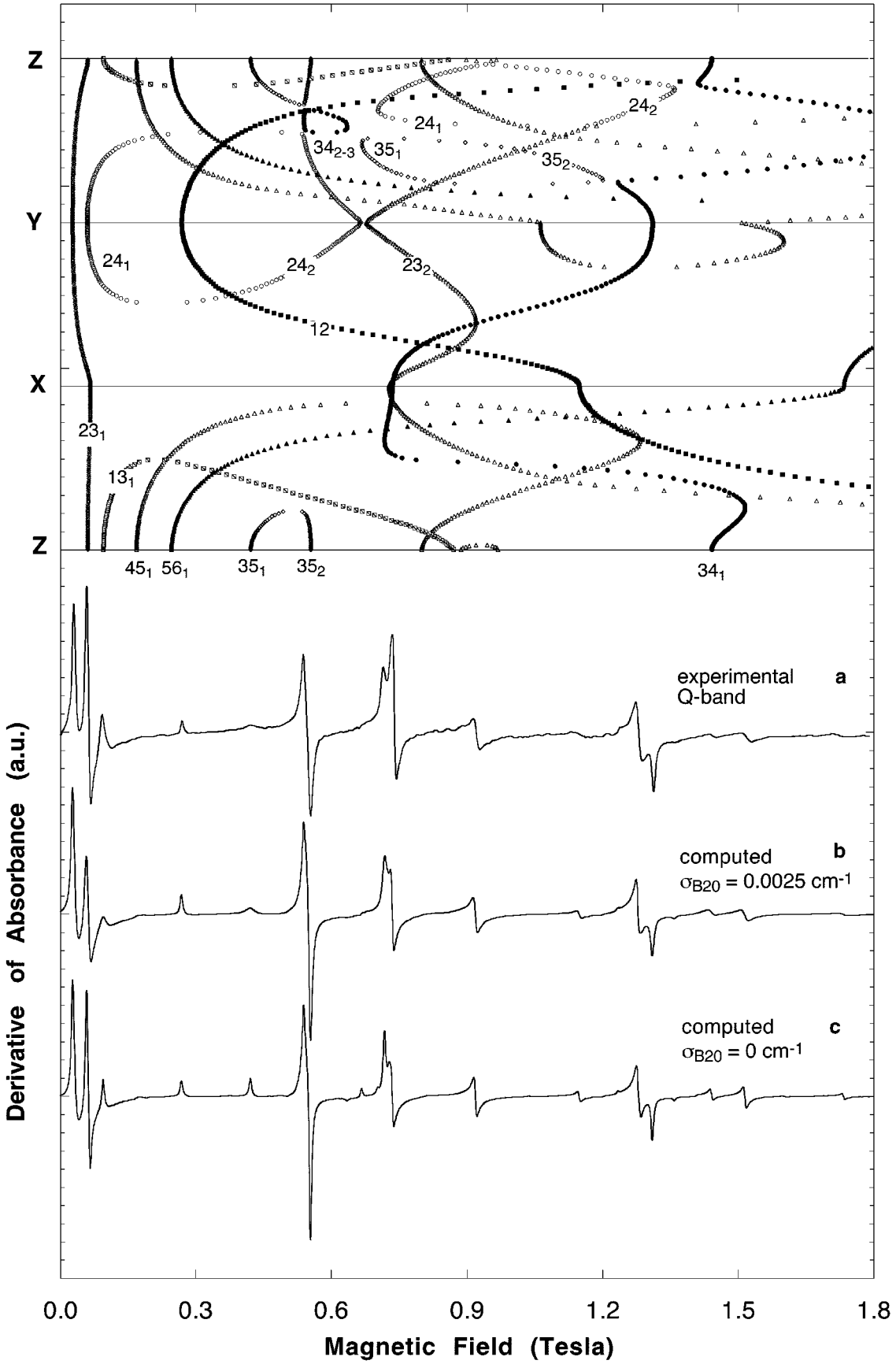
Z
Y
X
Z
24_1
24_2
34_{2-3}
35_1
35_2
24_1
24_2
23_2
12
23_1
13_1
45_1 56_1
35_1
35_2
34_1
experimental
Q-band
a
computed
σ_{B20} = 0.0025 cm^{-1}
b
computed
σ_{B20} = 0 cm^{-1}
c
Derivative of Absorbance (a.u.)
0.0
0.3
0.6
0.9
1.2
1.5
1.8
Magnetic Field (Tesla)

TABLE 6
Experimental and Calculated Line Positions (Tesla) for the Fe^{3+} Center in a Natural Polycrystalline Diaspore (Turkey) at 120 K

Transition		*X*-band (ν = 9.4240 GHz)		*Q*-band (ν = 34.0095 GHz)	
nm_p	[θ, ϕ]	Exp.	Calc.	Exp.	Calc.
12_1	*X*	0.3791	0.3791	1.1500	1.1487
12_1	*Y*	0.0731	0.0724	0.2703	0.2687
13_1	*Z*			0.0929	0.0952
23_1	*Y*			0.0298	0.0269
24_1	*Y*			0.0591	0.0590
34_1	*X*	0.1625	0.1614	0.7410	0.7350
34_1	*Y*	0.2012	0.2018	1.3129	1.3104
34_2	*Y*	0.5000	0.5004		
34_3	*Y*	0.8547	0.8526		
34_1	*Z*	0.1400	0.1394	1.4439	1.4417
34_1	(60, 180)			0.7130	0.7176
35_1	*Z*			0.4212	0.4211
35_2	*Z*			0.5570	0.5538
56_1	*Y*	0.8416	0.8423		

reasonable agreement is found when neglecting B_4^{-2} and B_4^{-4} parameters, i.e., when assuming an orthorhombic site symmetry instead of the true monoclinic site symmetry of the host site.

4.4.3. Triclinic site symmetry: Fe^{3+} in $\alpha Al(OH)_3$ (gibbsite). In the case of triclinic site symmetry, B_2^0, B_2^2, B_4^0, B_4^1, B_4^{-1}, B_4^2, B_4^{-2}, B_4^3, B_4^{-3}, B_4^4, and B_4^{-4} parameters are nonzero and no crystallographic symmetry axis exists. The *Z* axis is taken along the twofold axis of the second-order ZFS tensor, where $|B_2^0|$ is maximum. The *X* axis is chosen such that B_2^{-2} vanishes. These axes do not correspond to any symmetry axis of the fourth-order ZFS tensor and all fourth-order terms are nonzero. This situation corresponds to a full noncoincidence of the second- and fourth-order principal axis frames. In that case, the integration domain has to be extended to the whole half-sphere.

An example of such a complex situation is given by the EPR spectra of Fe^{3+} substituted for Al^{3+} in the gibbsite structure, $\alpha Al(OH)_3$. The gibbsite structure is characterized by dioctahedral layers containing two distorted octahedral Al sites, Al_1 and Al_2, both with triclinic site symmetry *1* (*60*). Both Al octahedra are defined by six hydroxyl groups with similar average Al–O distances, 1.902($\pm$0.005) Å and 1.905($\pm$0.005) Å, for Al(1) and Al(2) respectively, and have similar long-range environments. An *X*-band EPR powder spectrum of the Fe^{3+} center in gibbsite was first reported in (*61*), where the similarity of this spectrum to that of iron in kaolinite ($Si_2Al_2O_5(OH)_4$) was noticed. Recently, evidence of Fe^{3+} substitution at both triclinic Al sites in the dioctahedral layer of kaolinite has been demonstrated (*20*). Second-order Stevens constants and a computed *X*-band powder spectrum were reported. As shown in Fig. 7, the *X*-band powder spectrum of an iron-doped polycrystalline gibbsite sample is well modeled by considering the existence of two Fe^{3+} centers, referred to hereafter as A and B (Table 7). Those two sites are unambiguously distinguished at *Q*-band, where more than 40 sharp lines are observed (Fig. 8). The complexity of the *Q*-band spectrum of the Fe^{3+} centers in gibbsite sheds light on the necessity of fully computing EPR powder spectra and related angular dependencies in order to index experimental powder lines. Second- and fourth-order ZFS parameters for both A- and B-centers (Table 7) were refined by simultaneously adjusting *X*-band and *Q*-band line positions (Table 8). The large numbers of *Q*-band lines taken into account in the refinement, 23 and 9 for A- and B-centers respectively, allowed very good relative accuracy in second-order ZFS parameter values, $\leq$2‰ and $\leq$5‰ for A- and B-centers respectively, fourth-order ZFS parameter values being, however, less accurate (Table 7). Triclinic site symmetry is observed for the A-center, as indicated by the splitting of several lines at *Q*-band (Table 8). Especially, angular dependencies of the 35_1, 45_1, and 34_1 transitions differ between the *ZOX* and *ZO*$-$*X* planes and thus well constrain the B_4^3 value. In the same way, angular dependencies of both the 25_2 and 34_1 lines differ between the *XOY* and *XO*$-$*Y* planes and thus constrain the B_4^{-2} and B_4^{-4} values. Eventually, the complex angular dependency of the 34_1 line in the $g = 2$ region at *Q*-band constrains the B_4^1, B_4^{-1}, and B_4^{-3} values. The triclinic distortion of the A-center strongly supports that this center is related to Fe^{3+} ions substituted for Al^{3+} ions at Al(1) and/or Al(2) structural sites. For the B-center, line broadening, mainly due to site-to-site fluctuation of the ligand field ($\sigma_{B_2^0} = 0.003$ cm^{-1}), hinders the observation of any small splitting of angular dependencies of 34_1 or 45_1 transitions between the *ZOX* and *ZO*$-$*X* planes. As a consequence, the B-center was described in monoclinic site symmetry, the B_4^{-2} and B_4^{-4} values being well constrained by the splitting between the *XOY* and *XO*$-$*Y* angular dependencies of the 34_1 line at *Q*-band. The B-center likely corresponds to a structural site, with regard to the significant temperature dependence of its ZFS parameters (*62*), although its local symmetry has not been accurately determined. The lack of information about the relative orientation of the ZFS and the crystallographic coordinate

FIG. 6. Experimental and calculated *Q*-band powder spectra at 120 K of Fe^{3+} ions at Al site in natural diaspore from Turkey. Upper part: angular dependencies where transitions are labeled nm_p; lower part: (a) experimental spectrum; (b) computed spectrum with $\sigma_{B_2^0} = 0.0025$ cm^{-1} and $\Gamma_0 = 0.006$ T; (c) computed spectrum with $\sigma_{B_2^0} = 0$ cm^{-1} and $\Gamma_0 = 0.006$ T. Note that "looping" transitions, 13_{1-2}, 24_{1-2}, and 35_{1-2}, as well as the "true crossing" transitions, $24_2 - 23_2$, do not give rise to any "glitch" in the spectrum computed with strain effect (see Section 3.5).

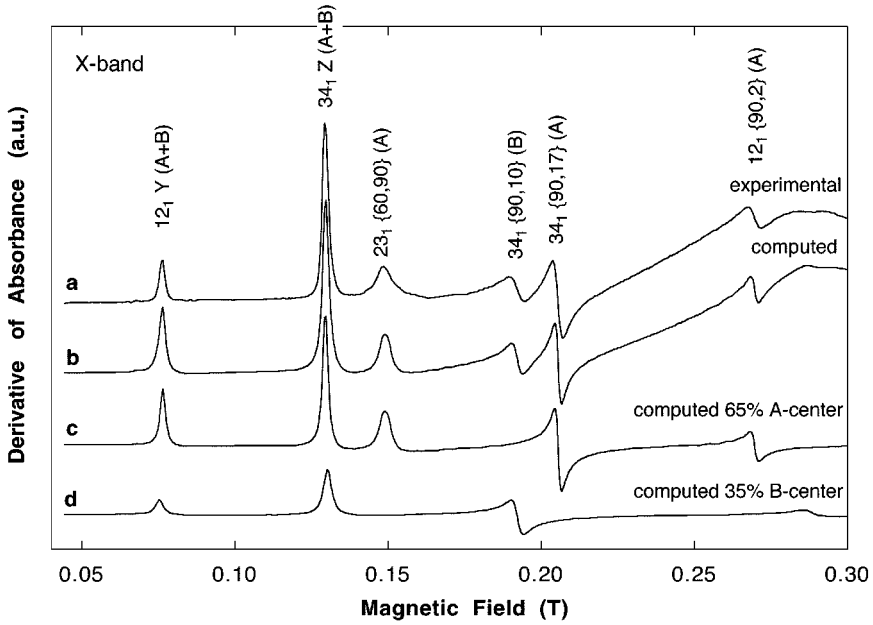

FIG. 7. Experimental and calculated *X*-band powder spectra at 300 K of Fe^{3+} ions in synthetic gibbsite (0.025 wt% Fe). (a) Experimental spectrum; (b) computed spectrum with 65% A-center and 35% B-center; a spline baseline, accounting for super-paramagnetic iron-oxide signals, has been added; (c) computed spectrum of A-center; (d) computed spectrum of B-center.

frames, respectively, hinders a crystallographic assignment of A- and B-centers in relation to Al(1) and Al(2) octahedra in the gibbsite structure.

Direct full-spectrum fitting was performed in order to determine the relative amounts of A- and B-centers in the gibbsite studied. Best fits at both frequencies were obtained by including 65 ± 5% and 35 ± 5% of A- and B-centers, respectively (Figs. 7, 8). Such an uneven site distribution may be related to easier relaxation processes for the A-center than for the B-center, as suggested by the significantly lower B_2^0 and $\sigma_{B_2^0}$ values for the A-center (0.0869 cm^{-1} and 0.0009 cm^{-1}, respectively) than for the B-center (0.1400 cm^{-1} and 0.003 cm^{-1}, respectively).

5. CONCLUSION

The present code is a powerful tool for interpreting EPR powder spectra. It is especially useful when dealing with spin Hamiltonians where the Zeeman, the fine structure, and/or the hyperfine structure terms have the same order of magnitude, because direct diagonalization of the full spin Hamiltonian is used. The development of an efficient algorithm for determining resonance fields, as well as the use of a fast algorithm for integrating angular dependencies over the orientation sphere, allows computation of smooth EPR powder spectra on wide field ranges within short CPU times. For instance, using an IBM RISK6000 43P computer, the computation of the *Q*-band powder spectrum of the Cr^{3+} center ($n = 4$) in α-Al_2O_3 (Fig. 1e) required 4 s CPU time with 50 steps in the *ZOX* plane, 3182 field steps of 0.0005 T, and a H_{limit} value of 1.0 T. In the same way, the computation of the *Q*-band powder spectrum of the A-Fe^{3+}-center ($n = 6$) in gibbsite (Fig. 8c) required 302 s CPU, with 5100 elementary triangles (integration on the half-sphere), 1791 field steps of 0.001 T, and an H_{limit} value of 0.05 T. The present examples demonstrate that accurate second- and fourth-order ZFS parameters as well as hyperfine parameters can be refined from EPR powder data, provided that *X*-band and *Q*-band data are fitted simultaneously. In addition, relative amounts of distinct centers can be easily determined. For instance, quantitative analysis of

TABLE 7
EPR Parameters (cm^{-1}) of A and B Fe^{3+} Centers at Al^{3+} Sites in a Synthetic Gibbsite at 300 K

	B_2^0	B_2^2	$60B_4^0$	$60B_4^1$	$60B_4^{-1}$	$60B_4^2$	$60B_4^{-2}$	$60B_4^3$	$60B_4^{-3}$	$60B_4^4$	$60B_4^{-4}$
A-center	0.0869	0.0480	−0.0027	−0.003	−0.014	0.033	−0.048	−0.045	−0.050	−0.014	−0.033
B-center	0.1400	0.0695	0.0141	0	0	0.008	−0.011	0	0	0.129	−0.065

Note. g value is taken isotropic at 2.0000; uncertainties are on the last digit.

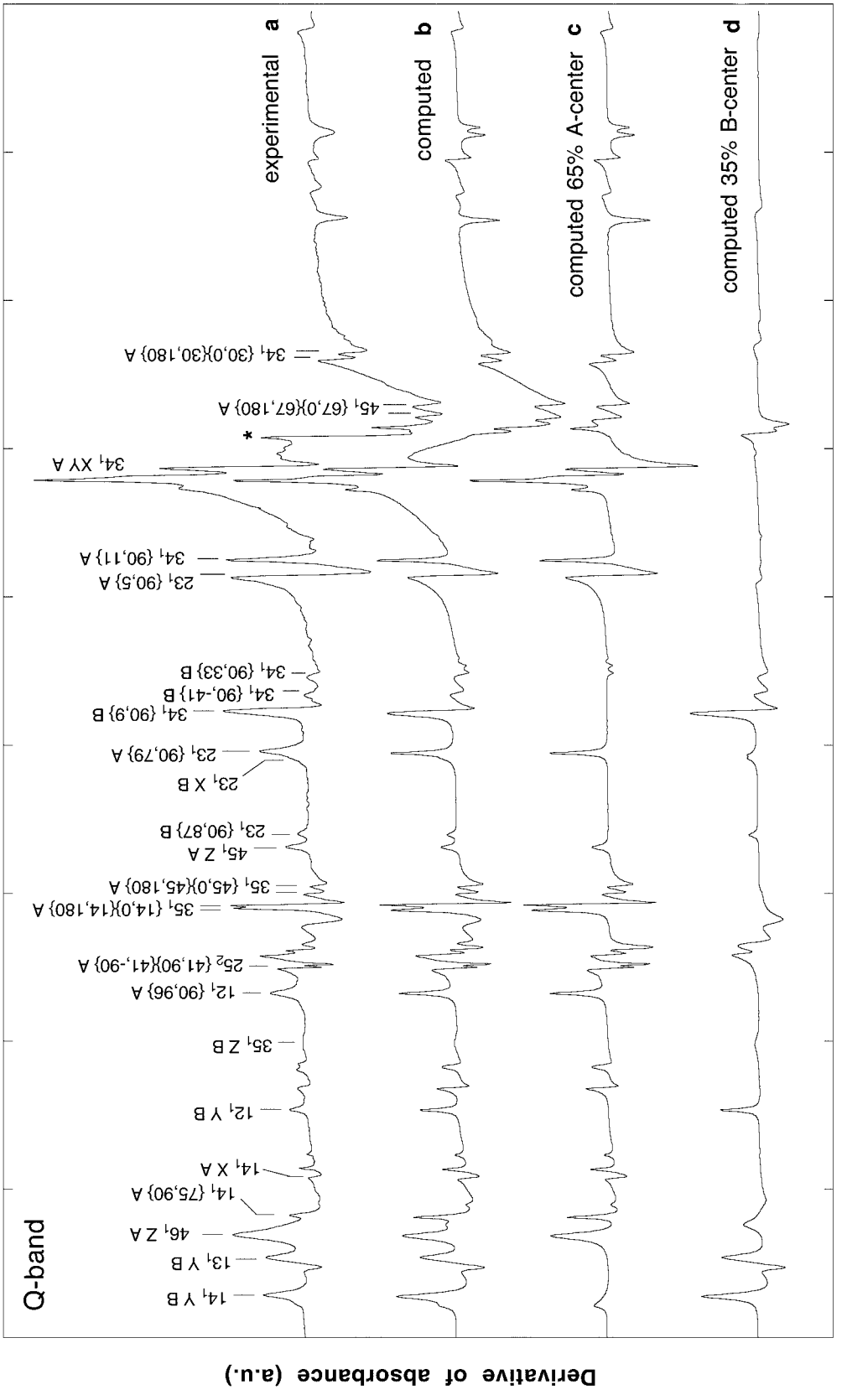

FIG. 8. Experimental and calculated *Q*-band powder spectra at 300 K of Fe^{3+} ions in synthetic gibbsite (0.025 wt% Fe). (a) Experimental spectrum; (b) computed spectrum with 65% A-center and 35% B center; a spline baseline, accounting for super-paramagnetic iron-oxide signals, has been added; (c) computed spectrum of A-center; (d) computed spectrum of B-center. The asterisk indicates an unidentified signal not related to Fe^{3+} and disappearing at low temperature (52).

TABLE 8
Experimental and Calculated Line Positions (Tesla) for the A- and B-Fe^{3+} Centers in Gibbsite[a]

Transition		*X*-band (ν = 9.4200 GHz)		*Q*-band (ν = 34.0040 GHz)	
nm_p	[θ, ϕ]	Exp.	Calc.	Exp.	Calc.
A-center					
34_1	*Z*	0.1288	0.1289		
23_1	{60, −90}	0.15	0.1489		
23_1	{60, 90}	0.15	0.1505		
34_1	{90, 17}	0.2062	0.2059		
12_1	{90, 2}	0.2707	0.2700		
46_1	*Z*			0.1378	0.1379
14_1	{75, 90}			0.1654	0.1640
14_1	{90, 0}			0.2165	0.2160
12_1	{90, 96}			0.4640	0.4651
25_2	{41, 90}			0.4986	0.4989
25_2	{41, −90}			0.5029	0.5029
35_1	{14, 0}			0.5785	0.5791
35_1	{14, 180}			0.5832	0.5856
35_1	{45, 0}			0.6005	0.6013
35_1	{45, 180}			0.6108	0.6110
45_1	*Z*			0.6624	0.6632
23_1	{90, 79}			0.7909	0.7906
23_1	{90, 5}			1.0288	1.0291
34_1	{90, 11}			1.0480	1.0498
34_1	{90, 178}			1.1444	1.1447
34_1	{90, 86}			1.1563	1.1570
34_1	{90, 63}			1.1650	1.1644
34_1	{90, −53}			1.1760	1.1758
45_1	{67, 0}			1.2436	1.2427
45_1	{67, 180}			1.2585	1.2487
34_1	{30, 0}			1.3200	1.3210
34_1	{30, 180}			1.3295	1.3293
B-center					
34_1	*Z*	0.1305	0.1305		
34_1	{90, 10}	0.1928	0.1926		
14_1	*Y*			0.0562	0.0547
13_1	*Y*			0.1069	0.1086
12_1	*Y*			0.3061	0.3077
35_1	*Z*			0.3970	0.3969
23_1	{90, 87}			0.6795	0.6790
23_1	*X*			0.7875	0.7884
34_1	{90, 9}			0.8475	0.8472
34_1	{90, −41}			0.8710	0.8712
34_1	{90, 33}			0.8950	0.8947

[a] Note that few powder lines lie along the principal axes.

complex multiple-center spectra, including more than five distinct radiation-induced defect centers ($S = \frac{1}{2}$; $I \leq \frac{3}{2}$), was recently performed on a set of borosilicate glasses (*50*). Finally, the first-order perturbation approach for computing site-to-site fluctuations of the spin Hamiltonian parameters appears to be useful for better understanding EPR lineshapes, in relation to structural disorder and structural relaxation phenomena. However, this approach may fail when dealing with $S > \frac{1}{2}$ centers in poorly ordered minerals and noncrystalline solids. In those cases, distributions of ZFS parameters are generally no longer Gaussian, but are asymmetric or exhibit multiple modes. Modeling EPR spectra of paramagnetic centers in such disordered materials requires multiple-spectra computation (*21*). Future extensions of the code are in progress and will concern nonlinear inversion methods for analyzing site distributions in poorly ordered materials. The source code of the program is available without charge to academic users from request to the authors, or at the following URL: http://www.lmcp.jussieu.fr/~morin/zfsfit.html.

APPENDIX

Stevens' operators $\mathbf{O}_k^{\pm q}$ correspond to linear combinations of tensor operators and can be written as follows (*31*):

$$\mathbf{O}_k^0 = O_k^0$$

$$\mathbf{O}_k^q = \frac{1}{2}\,(O_k^q + O_k^{-q})$$

$$\mathbf{O}_k^{-q} = \frac{1}{2i}\,(O_k^q - O_k^{-q})$$

where the $O_k^{\pm q}$ are the nonnormalized tensor operators given in (*63*). Algebraic forms of the $\mathbf{O}_k^q$ are written as follows (*33*):

$$\mathbf{O}_2^0 = 3\mathbf{S}_z^2 - \mathrm{S}(\mathrm{S}+1)$$

$$\mathbf{O}_2^1 = \frac{1}{4}\,[\mathbf{S}_z(\mathbf{S}_+ + \mathbf{S}_-) + (\mathbf{S}_+ + \mathbf{S}_-)\mathbf{S}_z]$$

$$\mathbf{O}_2^2 = \frac{1}{2}\,(\mathbf{S}_+^2 + \mathbf{S}_-^2)$$

$$\mathbf{O}_4^0 = 35\mathbf{S}_z^4 - (30\mathrm{S}^2(\mathrm{S}+1)^2 - 25)\mathbf{S}_z^2 - 6\mathrm{S}^2(\mathrm{S}+1)^2 + 3\mathrm{S}^4(\mathrm{S}+1)^4$$

$$\mathbf{O}_4^1 = \frac{1}{4}\,[(7\mathbf{S}_z^3 - (3\mathrm{S}^2(\mathrm{S}+1)^2 + 1)\mathbf{S}_z)(\mathbf{S}_+ + \mathbf{S}_-) + (\mathbf{S}_+ + \mathbf{S}_-)(7\mathbf{S}_z^3 - (3\mathrm{S}^2(\mathrm{S}+1)^2 + 1)\mathbf{S}_z)]$$

$$\mathbf{O}_4^2 = \frac{1}{4}\,[(7\mathbf{S}_z^2 - \mathrm{S}^2(\mathrm{S}+1)^2 - 5)(\mathbf{S}_+^2 + \mathbf{S}_-^2) + (\mathbf{S}_+^2 + \mathbf{S}_-^2)(7\mathbf{S}_z^2 - \mathrm{S}^2(\mathrm{S}+1)^2 - 5)]$$

$$\mathbf{O}_4^3 = \frac{1}{4}\,[\mathbf{S}_z(\mathbf{S}_+^3 + \mathbf{S}_-^3) + (\mathbf{S}_+^3 + \mathbf{S}_-^3)\mathbf{S}_z]$$

$$\mathbf{O}_4^4 = \frac{1}{4}\,(\mathbf{S}_+^4 + \mathbf{S}_-^4).$$

Algebraic forms of the $\mathbf{O}_k^{-q}$ are obtained from the above formulas by substituting $-i(\mathbf{S}_+^n - \mathbf{S}_-^n)$ for $(\mathbf{S}_+^n + \mathbf{S}_-^n)$. Matrix elements of $\mathbf{O}_2^0$, $\mathbf{O}_2^2$, $\mathbf{O}_4^0$, $\mathbf{O}_4^2$, $\mathbf{O}_4^3$, and $\mathbf{O}_4^4$ are tabulated in (*4*). The matrix elements of $\mathbf{O}_2^1$ and $\mathbf{O}_4^1$ are easily obtained from the matrix elements of O_2^1, O_2^{-1} and O_4^1, O_4^{-1}, respectively, tabulated in (*63*). The matrix elements of the $\mathbf{O}_k^{-q}$ are thoroughly obtained from those of the $\mathbf{O}_k^q$ as follows (*31*):

$$\langle m_S'|\mathbf{O}_k^{-q}|m_S\rangle = +i\langle m_S'|\mathbf{O}_k^q|m_S\rangle \quad \text{if } m_S' < m_S$$
$$\langle m_S'|\mathbf{O}_k^{-q}|m_S\rangle = -i\langle m_S'|\mathbf{O}_k^q|m_S\rangle \quad \text{if } m_S' > m_S.$$

According to these definitions, the ZFS term for $\mathrm{S} \leq \frac{5}{2}$ is written as

$$\mathbf{H}_{\mathrm{ZFS}} = \sum_{k=2,4} \sum_{q=-k}^{k} B_k^q \mathbf{O}_k^q$$

where the so-called Stevens constant, or ZFS parameters, B_k^q, are real. For instance, the matrix expression of $\mathbf{H}_{\mathrm{ZFS}}$ for $\mathrm{S} = \frac{5}{2}$ is written as

	$\left\vert +\frac{5}{2}\right\rangle$	$\left\vert +\frac{3}{2}\right\rangle$	$\left\vert +\frac{1}{2}\right\rangle$	$\left\vert -\frac{1}{2}\right\rangle$	$\left\vert -\frac{3}{2}\right\rangle$	$\left\vert -\frac{5}{2}\right\rangle$
$\left\langle +\frac{5}{2}\right\vert$	$10C_2^0 + C_4^0$					
$\left\langle +\frac{3}{2}\right\vert$	$-\sqrt{5}\,C_2^1$ $-\frac{1}{2\sqrt{5}}\,C_4^1$	$-2C_2^0 - 3C_4^0$				
$\left\langle +\frac{1}{2}\right\vert$	$\sqrt{10}\,C_2^2$ $+\frac{3}{2\sqrt{10}}\,C_4^2$	$-\sqrt{2}\,C_2^1$ $+\frac{1}{2\sqrt{2}}\,C_4^1$	$-8C_2^0 + 2C_4^0$			
$\left\langle -\frac{1}{2}\right\vert$	$-\frac{1}{2\sqrt{10}}\,C_4^3$	$3\sqrt{2}\,C_2^2$ $-\frac{1}{2\sqrt{2}}\,C_4^2$	0	$-8C_2^0 + 2C_4^0$		
$\left\langle -\frac{3}{2}\right\vert$	$-\frac{1}{\sqrt{5}}\,C_4^4$	0	$3\sqrt{2}\,C_2^2$ $-\frac{1}{2\sqrt{2}}\,C_4^2$	$\sqrt{2}C_2^1$ $-\frac{1}{2\sqrt{2}}\,C_4^1$	$-2C_2^0 - 3C_4^0$	
$\left\langle -\frac{5}{2}\right\vert$	0	$-\frac{1}{\sqrt{5}}\,C_4^4$	$\frac{1}{2\sqrt{10}}\,C_4^3$	$\sqrt{10}\,C_2^2$ $+\frac{3}{2\sqrt{10}}\,C_4^2$	$\sqrt{5}\,C_2^1$ $+\frac{1}{2\sqrt{5}}\,C_4^1$	$10C_2^0 + C_4^0$

where the upper triangular matrix is obtained by $\langle m'_S|\mathbf{H}_{ZFS}|m_S\rangle = \langle m_S|\mathbf{H}_{ZFS}|m'_S\rangle^*$ and where the C_k^q coefficients are related to the $B_k^{\pm q}$ ZFS parameters as follows:

$$C_2^0 = B_2^0$$

$$C_2^q = B_2^q + iB_2^{-q},\ q = 1, 2$$

$$C_4^0 = 60B_4^0$$

$$C_4^q = 60(B_4^q + iB_4^{-q}),\ q = 1, 2, 3, 4.$$

ACKNOWLEDGMENTS

The authors are indebted to Dr. B. Boizot and B. Dubertret for their help in programming. Dr. C. Brouder and Pr. F. Taulelle are congratulated for the interest they devoted to this work and for their help concerning theoretical and numerical aspects. The authors wish to thank Prof. G. Calas, Dr. Ph. Ildefonse, and E. Balan for clarifying discussions. Finally, the anonymous reviewers are acknowledged for their detailed and relevant remarks which improved the quality of this paper. This is contribution IPGP#1559.

REFERENCES

1. A. Weil, J. R. Bolton, and J. E. Wertz, "Electron Paramagnetic Resonance, Elementary Theory and Practical Applications," Wiley, New York (1994).
2. A. J. Hoff, "Advanced EPR in Biology and Biochemistry," Elsevier, Amsterdam (1989).
3. M. Ikeya, "New Applications of Electron Paramagnetic Resonance, Dating, Dosimetry and Microscopy," World Scientific, Singapore (1993).
4. A. Abragam and B. Bleaney, "Electron Paramagnetic Resonance of Transition Ions," Oxford Univ. Press, Oxford (1970).
5. J. R. Pilbrow, "Transition Ion Electron Paramagnetic Resonance," Clarendon Press, Oxford (1990).
6. R. Büscher, K. P. Such, and G. Lehman, Local relaxations around Fe^{3+} and Cr^{3+} in Al sites in minerals, *Phys. Chem. Minerals* **14,** 553–559 (1987).
7. G. Calas, Electron paramagnetic resonance, *in* "Spectroscopic Methods in Mineralogy and Geology" (Hawthorne, Ed.), Reviews in Mineralogy, Vol. 18, pp. 513–571, Mineral. Soc. Amer., Washington (1988).
8. J. M. Gaite, Study of the structural distortion around S-state ions in crystals, using the fourth-order spin-Hamiltonian term of the EPR spectral analysis, *in* "Electronic Magnetic Resonance of the Solid State" (J. A. Weil, Ed.), pp. 151–161, Can. Soc. Chem., Ottawa (1987).
9. P. C. Taylor, J. F. Baugher, and H. M. Kriz, Magnetic resonance spectra in polycrystalline solids, *Chem. Rev.* **75,** 204–238 (1975).
10. C. Chachaty and E. J. Soulié, Determination of electron spin resonance static and dynamic parameters by automated fitting of the spectra, *J. Phys. III France* **5,** 1927–1952 (1995).
11. J. W. Orton, "Electron Paramagnetic Resonance," Iliffe, London (1968).
12. N. N. Tikhomirova, S. N. Dobryakov, and I. V. Nikolaeva, The calculation of ESR spectrum of Mn^{2+} ions in polycrystalline samples, *Phys. Stat. Sol. (a)* **10,** 593–603 (1972).
13. R. D. Dowsing and J. F. Gibson, Electron spin resonance of high-spin d^5 systems, *J. Chem. Phys.* **50,** 294–303 (1969).
14. R. Aasa, Powder line shapes in the electron paramagnetic resonance spectra of high-spin ferric complexes, *J. Chem. Phys.* **52,** 3919–3930 (1969).
15. M. Y. Shcherbakova and V. E. Istomin, Calculation of EPR spectra of Fe^{3+} with high zero-field-splitting in polycrystalline materials, *Phys. Stat. Sol. (b)* **67,** 461–469 (1975).
16. C. R. Byfleet, D. P. Chong, J. A. Hebden, and C. A. McDowell, Calculation of EPR transition fields and transition probabilities for a general spin Hamiltonian, *J. Magn. Reson.* **2,** 69–78 (1970).
17. R. L. Belford and M. J. Nilges, Computer simulation of powder spectra, EPR Symposium, 21st Rocky Mountain Conference, Denver, CO (1979).
18. G. Van Veen, Simulation and analysis of EPR spectra of paramagnetic ions in powders, *J. Magn. Reson.* **30,** 91–109 (1978).
19. D. Wang and G. R. Hanson, A new method for simulating randomly oriented powder spectra in magnetic resonance: the *S*ydney *Op*era *H*ouse (SOPHE) method, *J. Magn. Reson. A* **117,** 1–8 (1995).
20. J. M. Gaite, P. Ermakoff, and J. P. Muller, Characterization and origin of two Fe^{3+} EPR spectra in kaolinite, *Phys. Chem. Minerals* **20,** 242–247 (1993).
21. C. Legein, J. Y. Buzaré, J. Emery, and C. Jacobini, Electron paramagnetic resonance determination of the local field distribution acting on Cr^{3+} and Fe^{3+} in transition metal fluoride glasses (TMFG), *J. Phys. Condens. Matter* **7,** 3853–3862 (1995).
22. A. B. Vassilikou-Dova and G. Lehman, EPR of V^{4+} and Fe^{3+} in titanites, *Phys. Chem. Minerals* **15,** 559–563 (1988).
23. S. K. Sur and T. F. Cooney, Electron paramagnetic resonance study of iron(III) and manganese (II) in the glassy and crystalline environments of synthetic fayalite and tephroite, *Phys. Chem. Minerals* **16,** 693–696 (1989).
24. J. M. Gaite and J. Michoulier, Application de la résonance paramagnétique électronique à l'étude de la structure des feldspaths, *Bull. Soc. fr. Minéral. Cristallogr.* **93,** 341–356 (1970).
25. J. Michoulier and J. M. Gaite, Site assignment of Fe^{3+} in low symmetry crystals. Application to $NaAlSi_3O_8$, *J. Chem. Phys.* **56,** 5205–5213 (1972).
26. J. M. Gaite, Etude des propriétés locales dans les cristaux de basse symétrie à l'aide de la RPE d'ions à l'état S, Ph.D. Thesis, University of Orleans (1973).
27. M. Razeghi, Contribution des spectres RPE de Mn^{2+}, Gd^{3+}, Eu^{2+} en solution dans $(PO_4)_2Pb_3$ à l'étude du changement de phase subi par ce cristal, Ph.D. Thesis, University of Paris-Sud (1979).
28. J. M. Gaite, Pseudo-symmetries of crystallographic coordination polyhedra. Application to forsterite and comparison with some EPR results, *Phys. Chem. Miner.* **6,** 9–17 (1980).
29. J. M. Gaite and S. S. Hafner, Environment of Fe^{3+} at the M2 and Si Sites of forsterite obtained from EPR, *J. Chem. Phys.* **80,** 2747–2751 (1984).
30. J. M. Gaite, A. S. Bookin, and V. Drits, Local distorsion of the spodumene structure around isolated cations using EPR and the superposition model, *Phys. Chem. Miner.* **12,** 145–148 (1985).
31. C. Rudowicz, Transformation relations for the conventional O_k^q and normalised O'^q_k Stevens operator equivalents with $k = 1$ to 6 and $-k \le q \le k$, *J. Phys. C: Solid State Phys.* **18,** 1415–1430 (1985).
32. K. W. H. Stevens, Matrix elements and operator equivalents connected with the magnetic properties of rare-earth ions, *Proc. Phys. Soc.* **65,** 209–215 (1952).
33. D. J. Newman and W. Urban, Interpretation of S-state ion spectra, *Adv. Phys.* **24,** 793–844 (1975).
34. C. P. Keijzers and E. de Boer, E.S.R. study of copper and silver *N,N*-dialkyldiselenocarbamates. Part II. Interpretation of spectra

measured in host lattices with monomeric structures, *Molec. Phys.* **29,** 1007–1020 (1975).

35. J. F. Stenger, Y. Dusaussois, G. Marnier, H. Rager, and J. M. Gaite, Electron paramagnetic resonance study of a new Fe^{3+} centre in $KTiOPO_4$, *J. Phys. Condens. Matter* **1,** 4643–4648 (1989).

36. J. Minge, M. J. Mombourquette, and J. A. Weil, EPR of Fe^{3+} in a-quartz: The sodium-compensated center, *Phys. Rev. B* **42,** 33–36 (1990).

37. M. J. Mombourquette and J. A. Weil, Simulation of magnetic resonance powder spectra, *J. Magn. Reson.* **99,** 37–44 (1992).

38. D. W. Alderman, S. M. Solum, and D. M. Grant, Methods for analyzing spectroscopic line shapes. NMR solid powder patterns, *J. Chem. Phys.* **84,** 3717–3725 (1986).

39. G. G. Belford, R. L. Belford, and J. F. Burkhalter, Eigenfields: A practical direct calculation of resonance fields and intensities for field-swept fixed-frequency spectrometers, *J. Magn. Reson.* **11,** 251–265 (1973).

40. LAPACK driver routine (version 2.0), Univ. of Tennessee, Univ. of California Berkeley, NAG Ltd. Courant Institute, Argonne National Lab, and Rice University, September 30, 1994.

41. E. Wasserman, L. C. Snyder, and W. A. Yager, ESR of the triplet state of randomly oriented molecules, *J. Chem. Phys.* **41,** 1763–1767 (1964).

42. R. S. DeBiasi and D. C. S. Rodriguez, Measurement of small concentrations of Cr and Fe in α-Al_2O_3 using electron spin resonance, *J. Am. Ceram. Soc.* **68,** 409–412 (1985).

43. A. Edgar and D. R. Hutton, Exchange-coupled pairs of Cr^{3+} ions in emerald. *J. Phys. C: Solid State Phys.* **11,** 5051–5063 (1978).

44. F. Holuj and A. Jesmanowicz, EPR of Fe^{3+} in andalusite and kyanite at V-band and the pair spectra, *Phys. Stat. Sol. (a)* **48,** 191–198 (1978).

45. R. F. Wenzel and Y. W. Kim, Linewidth of the electron paramagnetic resonance of $(Al_2O_3)_{1-x}(Cr_2O_3)_x$, *Phys. Rev.* **140,** 1592–1598 (1965).

46. J. R. Pilbrow, G. R. Sinclair, D. R. Hutton, and G. J. Troup, Asymmetric lines in field-swept EPR: Cr^{3+} looping transitions in ruby, *J. Magn. Reson.* **52,** 386–399 (1983).

47. R. W. Warren, EPR of Mn^{2+} in calcium fluorophosphate, *Phys. Rev. B* **2,** 4383–4388 (1970).

48. P. H. Kasai, Electron paramagnetic resonance study of Mn^{2+} ion in polycrystalline calcium fluorophosphate, *J. Phys. Chem.* **66,** 674–680 (1962).

49. Y. Ohkubo, Electron spin resonance spectra of divalent manganese ion in natural apatite single crystals, *J. Phys. Soc. Japan* **18,** 916–917 (1963).

50. B. Boizot, G. Petite, D. Ghaleb, and G. Calas, Radiation induced paramagnetic centers in nuclear glasses by EPR spectroscopy, *Nucl. Instr. Meth. Phys. Res. B* **141,** 580–584 (1998).

51. T. Kato, "Perturbation Theory for Linear Operators," 2nd edition, Springer Verlag, Berlin (1991).

52. F. X. Cabanas and C. F. Schwerdtfeger, Level-crossing effects in *N,N*-diethylmorpholinium tetracyanoquinodimethane. *Phys. Rev. B* **39,** 11241–11250 (1989).

53. J. V. Von Neumann and E. Wigner, Über das Verhalten von Eigenwerten bei adiabatischen Prozessen. *Physik. Zeitschr.* **30,** 467–470 (1929).

54. A. B. Roitsin, Generalized spin-Hamiltonian and low-symmetry effects in paramagnetic resonance, *Phys. Stat. Sol.* **104,** 11–35 (1981).

55. S. B. Garbow, K. E. Hillstrom, and J. J. More, Argonne National Laboratory. MINPACK Project, November 1996.

56. J. M. Gaite and C. Mosser, Experimental and modelized electron paramagnetic resonance spectra of Cr^{3+} in kaolinite, *J. Phys. Condens. Matter* **5,** 4929–4234 (1993).

57. G. S. Bogle and H. F. Symmons, Paramagnetic resonance of Fe^{3+} in sapphire at low temperatures, *Proc. Phys. Soc.* **73,** 531–532 (1959).

58. B. Boizot, Cristallochimie des éléments de transition fer, chrome et manganèse dans les alumines techniques, Ph.D. Thesis, University of Paris 6 (1996).

59. I. A. Gravilov, L. P. Litovkina, and M. L. Meil'man, EPR of imputity ions in single crystals of diaspore α-AlOOH, *Sov. Phys.—Solid State* **10,** 2177–2180 (1969).

60. H. Saalfeld and M. Wedde, Refinement of the crystal structure of gibbsite, $Al(OH)_3$, *Zeitschr. Kristallog.* **139,** 129–135 (1974).

61. J. P. E. Jones, B. R. Angel, and P. L. Hall, Electron spin resonance studies of doped synthetic kaolinite. II., *Clay Miner.* **10,** 257–269 (1974).

62. G. Morin, Cristallochimie du fer dans les bauxites, Ph.D. Thesis, Univ. of Paris 7 (1994).

63. H. A. Buckmaster, Tables of matrix elements for the operators $O_2^{\pm 1}$, $O_4^{\pm 1}$, $O_6^{\pm 1}$, $O_6^{\pm 5}$, *Can. J. Phys.* **40,** 1670–1677 (1962).